Check for updates

Perovskite oxides for electrocatalytic nitrogen/carbon fixation

Hui Zheng,[a] Wenping Li,[a] Siwei Ma,[a] Zheng Li,[a] Zhangxing Chen,[a] Longsheng Zhang, [ID] *[b] Jinguang Hu [ID] *[a] and Tianxi Liu [ID] *[b]

The electrochemical conversion of carbon and nitrogen species provides a sustainable way to reduce carbon dioxide emissions and address reactive nitrogen pollution. Perovskite oxides have shown broad application prospects in the field of electrocatalytic carbon/nitrogen fixation attributable to their tunable electronic structure, abundant oxygen vacancies and low cost. Their inherent ability to regulate electronic structure, defect states, and surface coordination environment enables them to selectively activate and convert inert molecules under mild conditions. This paper systematically reviews the progress of perovskite oxides in the field of electrocatalytic carbon/nitrogen fixation in recent years, with special emphasis on effective design strategies, including doping engineering, defect engineering, heterostructures and crystal face engineering. In addition, this work deeply analyzes the main challenges currently faced and proposes prospects for future development directions, including the precise design of high-performance catalysts, in-depth analysis of reaction mechanisms, stability improvement strategies, and the development of large-scale application technologies. By multidisciplinary cross-integration, perovskite oxide electrocatalysis technology holds great potential to contribute to carbon neutrality and green chemical synthesis, providing innovative solutions for sustainable development.

1 Introduction

The carbon and nitrogen cycles are fundamental biogeochemical processes that underpin the stability of Earth's ecosystems and support the sustainable development of human society.[1,2] Anthropogenic carbon dioxide (CO_2) emissions have become the primary driver of global climate change,[3] while the efficient transformation of nitrogen-containing species such as molecular nitrogen (N_2) and nitrate (NO_3^-) is essential for agriculture,

[a]Department of Chemical and Petroleum Engineering, University of Calgary, 2500 University Drive, NW, Calgary, Alberta T2N 1N4, Canada
[b]Key Laboratory of Synthetic and Biological Colloids, Ministry of Education, School of Chemical and Material Engineering, Jiangnan University, Wuxi 214122, China. E-mail: zhangls@jiangnan.edu.cn; jinguang.hu@ucalgary.ca; txliu@jiangnan.edu.cn

Hui Zheng received her master's degree from Jiangnan University in 2024. She is currently a PhD degree candidate at University of Calgary, with a research focus on electrocatalytic carbon and nitrogen conversion.

Hui Zheng

Zhangxing Chen is a founding chair professor at Eastern Institute of Technology, Ningbo. He got his PhD, MSc., and BSc from Purdue University, Xi'an Jiaotong University, and Nanchang (formerly, Jiangxi) University, respectively. He is a Fellow of both Royal Society of Canada and Canadian Academy of Engineering. He is a Member of U.S. National Academy of Engineering and a foreign Member of the Chinese Academy of Engineering. His research interests are reservoir engineering and renewable energy.

Zhangxing Chen

chemical production, and environmental protection.[4] As a result, the efficient fixation and utilization of carbon and nitrogen resources has emerged as a critical research focus across the fields of energy conversion, ecological preservation, and advanced materials development.

Traditional methods for converting CO_2 and nitrogen sources (N_2 and NO_3^-) include thermal catalysis, biological conversion, and chemical absorption. However, due to their problems such as extensive energy consumption and complex processes, it is difficult to achieve large-scale application.[5–7] Consequently, developing efficient, durable and highly selective catalytic systems to achieve efficient conversion and resource utilization of CO_2 and nitrogen sources has become a research hotspot in this field. Electrocatalysis is considered to be a key strategy to promote the green transformation of carbon and nitrogen cycles due to its controllable reaction pathway, clean energy-driving processes and excellent interfacial catalytic properties.[8–10]

Perovskite oxides have shown excellent performance and wide application potential owing to their unique crystal structure and highly adjustable chemical composition.[11] The diverse combination of cations at the A- and B-sites in perovskite oxides not only regulates the band structure and surface electronic state of the material, but also significantly affects the adsorption capacity of the catalyst for key reaction intermediates, thereby achieving precise regulation of the electrocatalytic

reaction path.[12,13] Compared with traditional precious metal catalysts, perovskite materials are low-cost, and have good chemical stability in alkaline and neutral environments, making them suitable for long-term electrolysis applications. In addition, the oxygen vacancies and adjustable metal oxidation states in perovskites provide additional active sites for reaction, improve interfacial electron and ion transport, and further improve the catalytic activity and product selectivity.[14] By adjusting the types and proportions of metal ions at the A- and B-sites (such as La, Sr, Mn, Ni, Fe, *etc.*), the intrinsic physicochemical properties of perovskite oxides can be modulated, thereby enhancing their electrocatalytic performance across multiple important reactions, including electrochemical reduction reactions of CO_2 (CO_2RR), N_2 (NRR), and NO_3^- (NO_3RR).[7,15–17] It is these unique advantages that make perovskite oxides an important candidate for efficient, stable, and economical electrocatalysts.

In recent years, with a deeper understanding of catalytic reaction pathways, adsorption behaviors, and intermediate evolution processes, perovskite oxides have shown significant progress in enhancing catalytic activity, reaction selectivity, and stability. Although some work has summarized perovskite oxides as electrocatalysts,[12,13] a comprehensive review specifically focusing on their application in carbon and nitrogen fixation reactions is still lacking. Systematically summarizing the research outcomes in these areas would clarify the structure–activity relationships across different material configurations and their electrocatalytic performance, thus providing theoretical support and innovative insights for the development of efficient and sustainable electrocatalytic systems. Moreover, such a review could promote advances in green energy conversion, chemical production and environmental remediation technologies, underlining its significant scientific importance and application value. This work provides a brief overview of perovskite oxide catalysts, with a particular focus on how their crystal structure and electronic configuration fundamentally influence catalytic performance. Key intrinsic factors such as non-stoichiometry, band structure, electron occupancy, and metal–oxygen interactions are discussed. On this basis, the research progress in multiple energy conversion fields is

Longsheng Zhang received his PhD degree from Fudan University. He is currently an associate professor at Jiangnan University. His research focuses on the design and synthesis of advanced materials for applications in energy conversion and storage.

Longsheng Zhang

Jinguang Hu received his PhD degree from the University of British Columbia. He is currently an associate professor and schulich research chair in the department of chemical and petroleum engineering at the University of Calgary, Canada. His main research interests include biomass valorization, sustainable energy and bio-inspired materials/systems for Energy, Environmental and Biomedical application.

Jinguang Hu

Tianxi Liu received his PhD degree from the Changchun Institute of Applied Chemistry, Chinese Academy of Sciences. He is currently a full professor at Jiangnan University. His main research interests include polymer nanocomposites, aerogels and their composites, and advanced materials for energy conversion and storage.
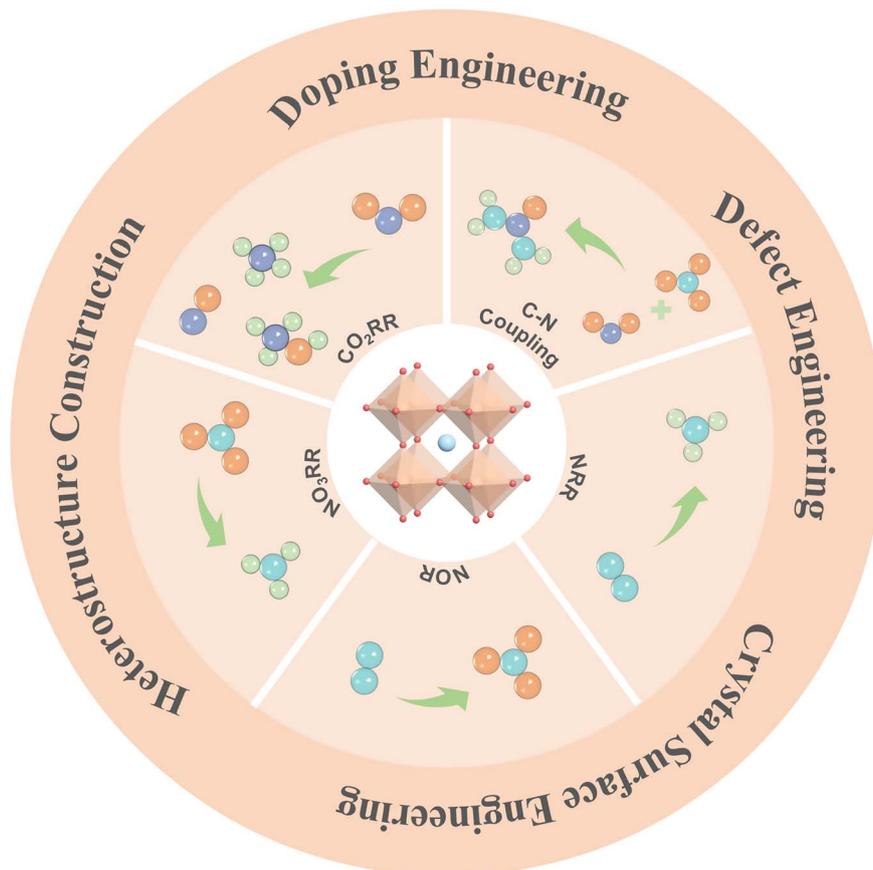
Tianxi Liu

Fig. 1 Schematic overview of perovskite oxides for electrocatalytic carbon and nitrogen fixation. The central ABO_3 lattice can be tailored through doping, defect engineering, crystal/surface modulation, and heterostructure construction, enabling improved activity and selectivity in CO_2RR, NO_3RR, NRR, NOR and C−N coupling. Cyan balls: nitrogen atoms. Hydrogen, carbon, and oxygen atoms are denoted by light green, blue, and orange spheres, respectively.

systematically reviewed, including CO_2RR, NRR, NO_3RR, NOR and electrocatalytic urea synthesis (Fig. 1). The discussion centers on critical aspects such as selectivity control, activity enhancement, and stability optimization. By integrating experimental studies with theoretical calculations, this work further summarizes prevalent performance modulation strategies, including doping engineering, defect regulation, facet control, and heterostructure construction. These strategies help elucidate the structure–activity relationships, offering both theoretical insights and practical guidance for the rational design and precise tuning of perovskite-based electrocatalysts. Finally, we point out the key challenges faced in current research and propose future development directions, which provide a theoretical basis and design ideas for the construction of efficient and stable perovskite oxide electrocatalysts, and are expected to promote the synergistic transformation and sustainable utilization of carbon and nitrogen resources.

2 Overview of the basics of perovskite oxide catalysts

Perovskite oxides (general formula: ABO_3) are a class of inorganic functional materials characterized by high structural

tunability and versatile electronic properties. They are widely used in gas sensors, solid oxide fuel cells and electrode materials, and have recently gained attention in the rapidly emerging field of electrocatalysis.[18–22] As shown in Fig. 2, the A-site is typically occupied by alkaline earth or rare earth metal ions (e.g., La, Sr, Ca, Ba), and the B-site by transition metal ions (e.g., Fe, Co, Ni, Mn, Ti, Mo).[14] The ideal perovskite crystal structure is usually cubic, oxygen atoms coordinate with the B-site metals to form a framework of $[BO_6]$ octahedra, and the A-site cations occupy the voids between these octahedra, contributing to structural stability and regulation of the material's electronic structure.[23] The B-site determines the intrinsic properties of the formed perovskite structure.[24]

2.1 Crystal structure

Due to factors such as ionic radius mismatch, uneven charge distribution and crystal field effect, the cubic structure of perovskite oxides often undergoes lattice distortion, presenting a variety of crystal forms such as tetragonal, orthorhombic and even hexagonal. In addition, the high flexibility of its composition has also led to the formation of a variety of perovskite oxide derivatives with ordered or layered structures, including double perovskite, quadruple perovskite, Ruddlesden–Popper
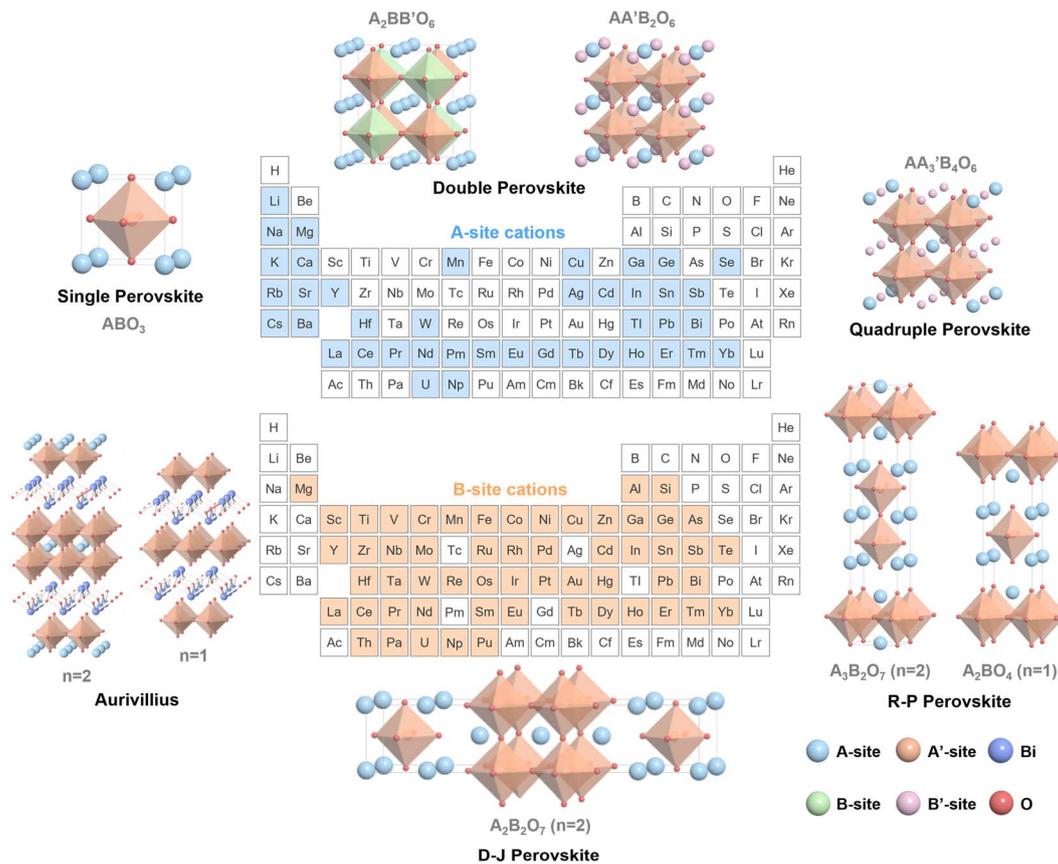
Fig. 2 Possible A-site and B-site cations for perovskite oxides highlighted in the periodic table, along with representative crystal structure schematics. The perovskite ABO_3 lattice consists of corner-sharing BO_6 octahedra with A-site cations in the interstitial positions. Structural flexibility enables various derivatives, including $A_2BB'O_6$ double perovskites, $AA'B_2O_6$ layered structures, and Ruddlesden–Popper phases. The broad compositional space of A-site (alkaline earth, rare-earth, and alkali metals) and B-site (transition metals, main group elements) cations provides abundant opportunities to tailor electronic structure, oxygen vacancy concentration, and lattice distortion, which are crucial for catalytic performance.

(R–P), Dion–Jacobson (D–J) and Aurivillius (Fig. 2). The distortion of the perovskite oxide structure and the formation of derivative phases help regulate the electronic structure and active sites, thereby enhancing catalytic activity and selectivity. Moreover, layered or ordered structures can improve ion/electron transport and structural stability, making them promising for more complex reaction environments. The distortion trend and formation tendency of these structures are closely related to the ionic size of the constituent elements, and can usually be predicted and evaluated by the Goldschmidt tolerance factor, t, which is defined as:[25] $t = \dfrac{r_A + r_O}{\sqrt{2}(r_B + r_O)}$, where r_A, r_B and r_O are the ionic radii of the A-site, B-site and O-ion, respectively. When the tolerance factor t is close to 1, the perovskite structure tends to exhibit ideal cubic symmetry.[26] When $t < 1$, the A-site cation is relatively small, leading to the rotation and tilting of the $[BO_6]$ octahedra and resulting in distorted structures such as orthorhombic or rhombohedral phases.[27,28] Conversely, when $t > 1$, the A-site cation is relatively large, which expands the lattice and distorts the octahedra, potentially causing the B-site cation to deviate from the octahedral center and form a polar structure. The tolerance factor is

a simple yet effective descriptor widely used in the design and phase prediction of perovskite materials.[27,28]

2.2 Nonstoichiometry

In ideal perovskite oxide structures, the stability of the crystal is not only influenced by the ionic radius matching of the A- and B-site cations but is also closely related to the overall charge neutrality, where the total charges of cations and oxygen anions must remain balanced. Even in non-stoichiometric systems, such charge neutrality is typically maintained through adjustments in the metal oxidation states, the introduction of defects, or carrier compensation mechanisms.[14] However, in actual materials, perovskite oxides often exhibit significant non-stoichiometry, such as oxygen vacancies, metal site defects, and mixed valence states of the B-site metal.[7,15] This deviation from the ideal composition can impart unique electrochemical activities to the material. The formation of non-stoichiometry is closely related to a variety of external factors, such as high temperature treatment, atmosphere adjustment (reducing or oxidizing environment), and heterovalent element doping.[29–31] These methods can induce the generation of oxygen vacancies,

changes in the local coordination environment, and the redistribution of the valence state of the B-site metal, thereby regulating the electronic structure and defect (oxygen vacancy and cation defect) concentration of the material.[32] For example, the introduction of oxygen vacancies regulates the electron density of the B-site metal and significantly improves its adsorption capacity for reaction intermediates, which is beneficial to the intermediate state stability and the electrocatalytic reaction activity. The formation of mixed-valence states at the B-site (*e.g.*, Fe^{3+}/Fe^{4+}, Co^{2+}/Co^{3+}) is a typical manifestation of non-stoichiometric regulation. Adjusting the oxygen partial pressure or doping with aliovalent metals enables the coexistence of multiple valence states, which helps maintain charge neutrality and structural stability, enhances electronic conductivity, facilitates interfacial charge transfer, and improves reaction kinetics.[33] It should be noted that although the enhancement of non-stoichiometry brings performance advantages, its excessive accumulation may also cause stability problems such as crystal structure collapse and metal ion dissolution. Therefore, precise control of defect concentration is the key to constructing highly active and highly stable catalysts. In general, non-stoichiometry, as an important feature that distinguishes perovskite oxides from other oxide materials, provides abundant reactive sites, good charge/ion migration capabilities, and structural flexibility to cope with complex reaction conditions. By rationally regulating the synthesis conditions, oxygen partial pressure environment, and element doping strategies, the engineering design of non-stoichiometry can be effectively achieved, providing a solid foundation for improving the performance of perovskite oxides in various electrocatalytic reactions such as CO_2RR and NO_3RR. The specific mechanisms of the effects of non-stoichiometry on electrocatalytic activity, selectivity, and stability will be discussed in detail in Sections 6.1 and 6.2.

2.3 Key indicators of electrocatalytic performance

2.3.1 e_g Orbital filling degree.
The metal ions in perovskite oxides are connected by oxygen bridges to form a metal–oxygen–metal structure, where the d orbitals split into t_{2g} and e_g orbitals. The e_g orbitals point directly toward the coordinating oxygen atoms and strongly overlap with the orbitals of reaction intermediates, making them crucial for reactant adsorption and activation. The e_g orbital filling significantly influences adsorption strength and electron transfer behavior, thereby playing a decisive role in electrocatalytic performance. Studies have shown that a higher e_g filling degree leads to excessive occupation of the antibonding orbital (σ^*), thereby weakening the bonding strength between the metal and the reactant and being detrimental to the effective activation of the reactant. In contrast, a lower e_g filling degree means fewer electrons on the antibonding orbital, which helps to form a stronger metal–reactant bond and enhances adsorption capacity. Additionally, excessively strong adsorption might hinder the desorption of reactants, thereby inhibiting the reaction process. The regulation of e_g orbital filling not only depends on the selection of the transition metal element at the B-site, but is also affected by many factors such as the synthesis method of the catalyst,

heterogeneous element doping, and reaction atmosphere.[34–36] Reasonable design of these parameters can achieve fine regulation of the electronic structure, thereby optimizing the catalytic performance. Density functional theory (DFT) calculations provide an important theoretical basis for revealing the activity–structure relationship between the e_g filling degree and catalytic activity, while characterization techniques such as X-ray photoelectron spectroscopy (XPS) and X-ray absorption fine structure (XAFS) experimentally verify the distribution of electronic states and orbital occupancy, further deepening the understanding of the catalytic mechanism.

In summary, rationally regulating the e_g orbital filling degree of perovskite oxides can optimize the adsorption capacity and reaction pathway and selectivity, thus improving the efficiency of electrocatalytic reactions, which is a critical strategy for perovskite oxide catalyst design.

2.3.2 B–O bond energy and covalency.
B–O bond energy and covalency play a vital role in the electrocatalytic reaction of perovskite oxides, profoundly affecting the activity and reaction mechanism of the catalyst. B–O bond energy directly determines the formation energy of oxygen vacancies. Weaker B–O bonds are more likely to introduce oxygen vacancies,[30] which are often considered as the key active sites in reactions such as CO_2RR and NO_3RR by enhancing reactant activation through optimized surface adsorption. In addition, the covalency of the B–O bond reflects the orbital hybridization strength between transition metals and oxygen. Moderately enhanced covalency can increase the degree of metal–oxygen electronic coupling to improve the efficiency of electronic conduction, thereby accelerating the interfacial electron transfer process and promoting reaction rate.[37] For instance, Grimaud *et al.* pointed out that the intrinsic electronic structure of transition metal oxides (covalent interactions between metal and oxygen) not only determines the catalytic activity of the oxygen evolution reaction (OER), but also profoundly affects its reaction mechanism.[38] Jiang *et al.* investigated the relationship between the removal efficiency of bisphenol A (BPA) and metal–oxygen covalency using $LaMnO_3$ perovskite oxide as the catalyst.[39] Experimental results showed that with increased metal–oxygen covalency, the charge transfer rate on the catalyst was enhanced, along with improved adsorption capacity for BPA and reaction intermediates. On the contrary, if the covalency is too weak, the d–p hybridization is insufficient, weakening the catalytic activity. Briefly, by optimizing the B–O bond energy and covalency *via* regulating the type of B-site metal, doping strategy and reaction atmosphere, the catalytic efficiency and product distribution of perovskite oxides in electrocatalytic reactions such as CO_2RR and NRR can be significantly improved, making it another important design parameter for constructing high-performance catalysts.

2.3.3 Metal–oxygen–metal bridge (B–O–B) angle.
In addition to the factors mentioned above, the metal–oxygen–metal bridge (B–O–B) angle is also a crucial factor affecting the catalytic performance of perovskite oxide catalysts, which determines the degree of orbital overlap between metal atoms, influencing electronic conduction and reactant adsorption.[40] In fact, the change in the B–O–B angle is essentially

a manifestation of lattice distortion. In electrocatalytic reactions, an optimal B–O–B angle can enhance the electronic coupling of metal–oxygen–metal, facilitating electron transport and the effective adsorption and conversion of reactants, thereby boosting catalytic activity. By precisely tuning the B–O–B angle, the electronic structure, active site exposure, and reaction pathway of the catalyst can be optimized, enabling fine control over its catalytic performance. An excessively small or large B–O–B angle may lead to structural instability or weakened electronic coupling, reducing catalytic performance. In conclusion, optimizing the B–O–B angle is of great significance for improving the electrocatalytic performance of perovskite oxide catalysts and is an efficient strategy for designing efficient catalysts. Although the effects of lattice distortions as a whole on perovskite oxides have been extensively studied, systematic investigations specifically focusing on the individual tuning of the B–O–B bond angle and its impact on electrocatalytic performance remain limited, and the related regulatory mechanisms are yet to be thoroughly understood.[41] lacking detailed mechanistic insights into how this parameter governs catalytic behavior. All in all, the catalytic performance of perovskite oxides depends on the fine regulation of these parameters. By optimizing these factors, the efficiency and selectivity of the catalyst can be improved, and the effective electrocatalytic reaction can be promoted.

3 Application of perovskite oxides in electrocatalytic nitrogen fixation

3.1 Electrocatalytic nitrogen reduction

The electrocatalytic NRR is a green technology that converts N_2 into ammonia (NH_3) under mild conditions, showing important implications for energy and environment.[42] However, it is extremely challenging to activate N_2 molecule under mild conditions owing to its strong N≡N triple bond (bond energy of about 941 kJ mol^{-1}).[43] Therefore, designing efficient NRR catalysts and establishing a thorough understanding of the reaction mechanisms are paramount to achieving efficient NH_3 synthesis.

In the electrocatalytic NRR process, the reaction generally occurs on the catalyst surface *via* sequential proton–electron transfer (H^+/e^-). First, N_2 is adsorbed at the active sites of the catalyst, forming adsorbed $*N_2$. Based on this, NRR can proceed *via* two main pathways: the associative pathway and the dissociative pathway. The associative mechanism can be classified
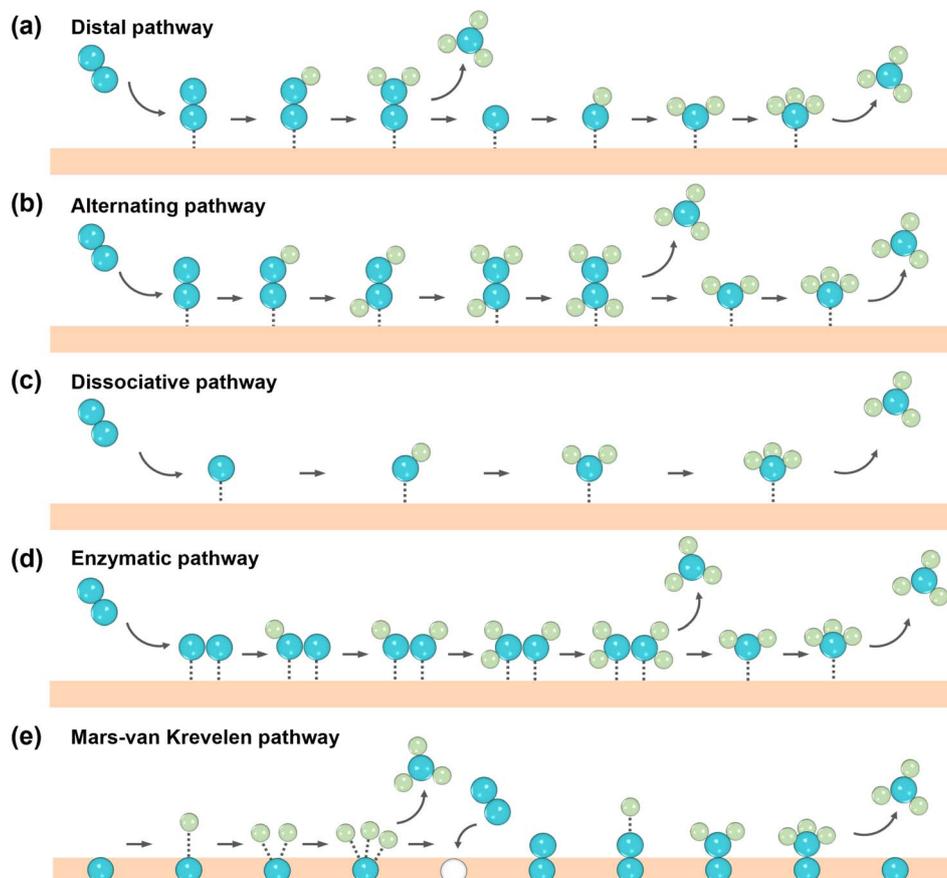

Fig. 3 Reaction mechanisms diagram of NRR. (a) Distal associative pathway; (b) alternating associative pathway; (c) dissociative pathway; (d) enzymatic dual-atom adsorption pathway; (e) Mars–van Krevelen pathway on transition-metal nitrides involving lattice N. Cyan balls: nitrogen atoms. Light green balls: hydrogen atoms. Cyan balls denote N atoms and light-green balls denote H atoms, arrows indicate sequential proton–electron transfer steps.

into a distal pathway (Fig. 3a) and an alternating pathway (Fig. 3b), depending on the sequence in which the two N atoms are hydrogenated. In the distal mechanism, one nitrogen atom preferentially accepts proton–electron pairs, gradually generating NH_3 and desorbing, leaving a single *N intermediate to continue reduction to produce a second NH_3 molecule.[44,45] In the alternating mechanism, the two nitrogen atoms alternately accept proton–electron pairs, proceeding stepwise until both are converted into NH_3.[46–48] In the dissociative pathway, as shown in Fig. 3c, N_2 initially dissociates into two *N intermediates on the catalyst surface, which are then protonated separately to produce NH_3.[49,50] However, this pathway generally requires higher energy. In addition to the case of single N atom adsorption, an enzymatic mechanism has been proposed (Fig. 3d), in which two N atoms are simultaneously adsorbed on the catalyst surface and are hydrogenated sequentially to generate and release NH_3.[51,52] In addition, the researchers proposed that NRR on transition metal nitrides can proceed via a new Mars–van Krevelen mechanism: H addition first acts on the lattice nitrogen on the surface to generate and release NH_3, and then the formed nitrogen vacancies adsorb N_2 and continue hydrogenation along the distal mechanism (Fig. 3e).[53] Overall, a deep exploration of the N_2 adsorption configuration, the energy barrier of the initial protonation step, and the stability of key intermediates is crucial for elucidating the NRR mechanism and guiding catalyst design optimization.

It is worth noting that these mechanistic pathways are closely related to the intrinsic structural features of perovskite oxides. For the distal pathway, the selective hydrogenation of one nitrogen atom relies on the adsorption preference of active sites, which can be effectively tuned by the e_g orbital occupancy of B-site transition metals and the presence of oxygen vacancies that modulate local electron density. In the alternating pathway, where two nitrogen atoms are hydrogenated in turn, a more symmetric adsorption configuration is required. The adjustable A/B-site ionic radii and the flexible B–O–B bond angles in perovskites help stabilize such bridge-like adsorption states, thereby facilitating the alternating mechanism. In the dissociative pathway, the initial cleavage of the strong N≡N bond demands highly reactive sites. Surface reconstruction and lattice oxygen participation in perovskites can provide such high-energy centers, enabling N≡N bond scission through Mars–van Krevelen-type processes. These correlations illustrate how the structural tunability of perovskite oxides may govern the preference for different NRR pathways and highlight their unique advantages compared with conventional catalysts.

Perovskite oxides have been applied in the field of electrocatalytic NRR due to their unique properties (Table 1). The first study on perovskite oxide for NRR research was reported in 2019,[62] which co-doped Cs and Ni into $LaFeO_3$ perovskite to introduce abundant oxygen vacancies enabled the electrochemical reduction of N_2 molecules in a two-electrode system (Fig. 4a). This work confirmed for the first time the electrocatalytic activity of perovskite oxides in NRR and expanded its application prospects in the field of electrocatalytic nitrogen fixation. Thereafter, researchers have done a lot of work to enhance the NRR performance of perovskite oxides. For example, Liu et al. introduced oxygen vacancies into $LaCoO_3$ (Vo-$LaCoO_3$) by plasma treatment, using Co atoms and their adjacent oxygen vacancies as active centers to synergistically activate N_2, where the faradaic efficiency (FE) of NH_3 reached 7.6% and the yield was 10.7 mmol $g_{cat.}^{-1}$ h^{-1}.[61] Mechanistic studies (Fig. 4b) show that many localized electrons accumulate at the oxygen vacancies in the $LaCoO_3$ catalyst, which is conducive to the transfer of electrons from the catalyst to the antibonding orbital of the N_2 molecule, thereby improving the NRR activity. Chu et al. reported a general strategy to enhance NRR activity by regulating oxygen vacancies induced by A-site defects in perovskite oxides (Fig. 4c), where the NH_3 yield of $La_{0.9}FeO_3$ reached 1.3 mmol $g_{cat.}^{-1}$ h^{-1} and FE reached 25.6%.[15] This work confirmed that the oxygen vacancy content is proportional to the A-site defects and the NRR activity is positively correlated with the oxygen vacancy content. Bastia et al. designed and synthesized a $NiTiO_3$-based nano-electrocatalyst that leveraged the synergistic characteristics of perovskite structures, including abundant oxygen vacancies, highly active Ni metal sites, and a built-in dipole moment from their noncentrosymmetric nature, which facilitates charge separation for N_2 activation.[60] To further enhance performance, ultrasmall metal nanocrystals were introduced as co-catalysts, forming

Table 1 Electrocatalytic NRR performance of perovskite oxides[a]

	Electrocatalyst	Electrolyte	Working electrode	Reactor	Potential (V vs. RHE)	NH₃ yield rate (mmol $g_{cat.}^{-1}$ h^{-1})	FE (%)	Ref.
1	$La_{0.9}FeO_{3-\delta}$	0.1 M Li_2SO_4	Carbon paper	H-cell	−0.3	1.3 (−0.5 V vs. RHE)	25.6	15
2	$LaCrO_3$	0.1 M Na_2SO_4	Carbon paper	H-cell	−0.8	1.55	15.0	54
3	$LiNbO_3$@MIL-0.4	0.1 M Na_2SO_4	Carbon paper	H-cell	−0.45	2.7	86.4	55
4	Vo-$LaFeO_3$ nanofiber	0.1 M HCl	Carbon paper	H-cell	−0.55	1.1	8.8	56
5	V_O-$BiFeO_3$	0.1 M K_2SO_4	Glassy carbon	Single-chamber cell	−0.4	5.3	13.5	57
6	$La_{0.5}Sr_{0.5}FeO_{3-\delta}$	0.1 M Na_2SO_4	Carbon paper	N/A	−0.6	0.7	0.5	58
7	$Ce_{1/3}NbO_3$	0.1 M Na_2SO_4	Carbon paper	H-cell	−0.8	10.34 μg h^{-1} cm^{-2}	6.8	59
8	Pt-$NiTiO_3$	0.1 M Na_2SO_4	Carbon paper	H-cell	−0.097	0.8 (−0.003 V vs. RHE)	27.0	60
9	Vo-$LaCoO_3$	0.1 M Na_2SO_4	Glassy carbon	H-cell	−0.6	10.7 (−0.7 V vs. RHE)	7.6	61

[a] Note: the yield rates reported in different studies were normalized using various method. Since some publications did not provide sufficient parameters for unit conversion, the values are presented only to indicate general levels and trends, rather than for strict numerical comparison, so as to avoid potential misinterpretation arising from inconsistent normalization.
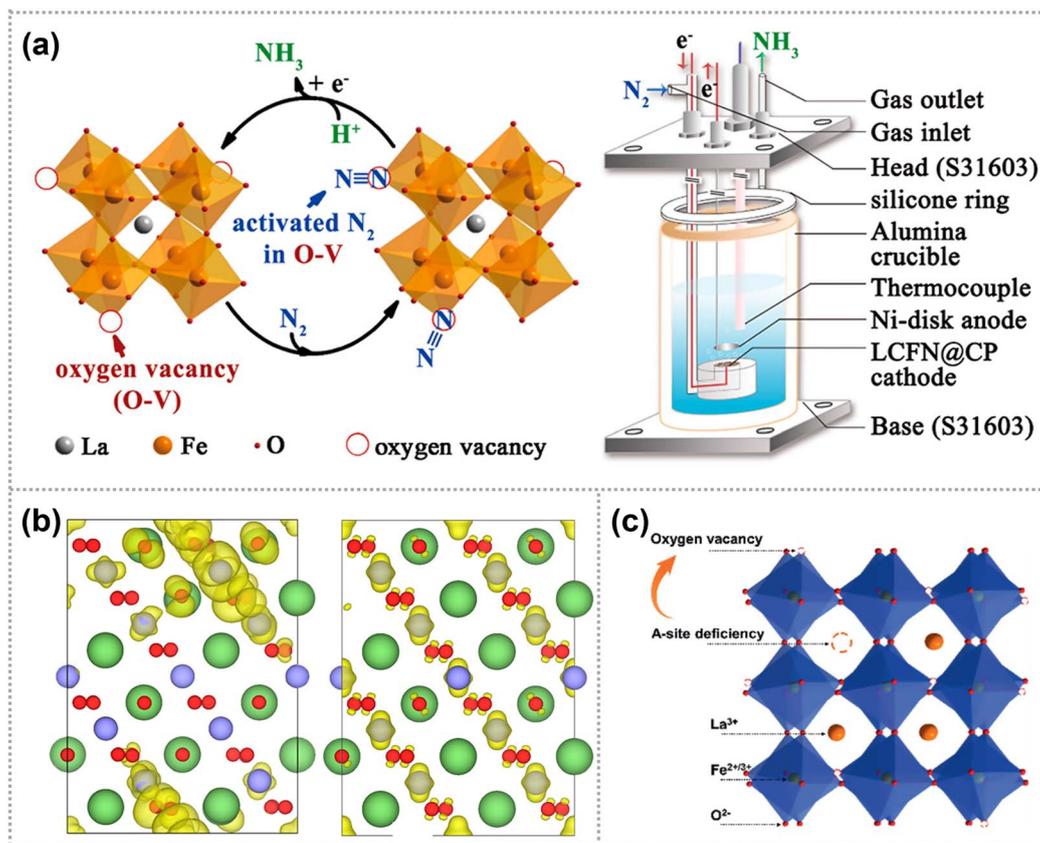
Fig. 4 (a) Schematic diagram of $La_aCs_bFe_cNi_dO_{3-\delta}$-catalyzed NRR.[62] Copyright 2019, American Chemical Society. (b) Partial charge density at the valence band edge of $LaCoO_3$ with (left) and without (right) oxygen vacancies, highlighting vacancy-induced electron localization.[61] Copyright 2019, American Chemical Society. (c) Schematic illustration of the generation of oxygen vacancies in A-site-deficient La_xFeO_3.[15] Copyright 2021, Wiley VCH GmbH.

heterogeneous interfaces that improved electron transfer, facilitated N_2 activation, and significantly reduced the required overpotential. The incorporation of noble metal heteroatoms (*e.g.*, Pd, Pt), due to their high electron affinity, induced charge redistribution and increased positive charge density on adjacent atoms, thereby enhancing N_2 chemisorption. Furthermore, the presence of multivalent species (Pd^{2+}, Pt^0, Pt^{2+}) and the jointly generated oxygen vacancies at the $NiTiO_3$/co-catalyst interface synergistically enhanced the NRR performance. In summary, perovskite oxides exhibit excellent activity and selectivity in the electrochemical NRR due to their structural diversity and rich defect engineering strategies. Through defect modulation, oxygen vacancy introduction, and heterointerface construction, the adsorption and activation of N_2 molecules are significantly enhanced, lowering the reaction energy barriers and thereby improving NH_3 yield and FE.

3.2 Electrocatalytic nitrate reduction

In the electrocatalytic NO_3RR, NO_3^- is first adsorbed and activated on the catalyst surface, forming intermediates such as $*NO_2$ or $*NO$. Subsequently, through the gradual transfer of electrons and protons, $*NO$ is further reduced to $*NH_2$, and ultimately NH_3 or NH_4^+ are generated and released into the electrolyte.[63–65] Key steps include the initial reduction of NO_3^- to $*NO_2$, bond cleavage and protonation of $*NO$, and the desorption of $*NH_2$ to form NH_3.[66–68] The electronic structure, adsorption strength and ability to regulate intermediates of the catalyst determine the reaction pathway and energy barriers, thereby influencing the NH_3 production rate and FE. Perovskite oxides exhibit unique advantages in NO_3RR due to their rich and adjustable A-site and B-site metal compositions, and stable crystal structures. The reported electrocatalytic NO_3RR performance of perovskite oxide is summarized in Table 2.

High-entropy perovskite oxides are multi-component solid solution materials based on the ABO_3 structure, in which the A-site and/or B-site are occupied by multiple principal elements, giving rise to a configurational entropy (ΔS_{mix}) of ≥ 1.5 R. Under the stabilization of the high-entropy effect, these materials can form a single-phase perovskite lattice. Through high-entropy engineering, the incorporation of multiple metal elements constructs a complex yet stable local environment, which not only enhances the tunability of the electronic structure but also introduces multi-site synergistic effects and abundant active centers, thereby significantly improving catalytic activity and product selectivity.[79–82] Guo *et al.* proposed a method to regulate the electronic spin state of Co through the A-site high-entropy management strategy.[75] Specifically, in the high-entropy

Table 2 Electrocatalytic NO$_3$RR performance of perovskite oxides

	Electrocatalyst	Electrolyte	Potential (V vs. RHE)	Reactor	Working electrode	NH$_3$ yield rate (mmol g$_{cat.}^{-1}$ h^{-1})	FE (%)	Ref.
1	La$_2$Cu$_{0.95}$Co$_{0.05}$O$_4$	0.5 M Na$_2$SO$_4$ + 1000 ppm KNO$_3$	−0.8	Single cell	Carbon paper	32.6 (−1.0 V vs. RHE)	93.2	69
2	La(MnFeCoCuZn)$_{0.2}$O$_3$	1 M NaOH + 0.5 M NaNO$_3$	−1.1	H-cell	Carbon cloth	18.6	98.7	70
3	LaFe$_{0.9}$Cu$_{0.1}$O$_{3-\delta}$	0.5 M Na$_2$SO$_4$ + 50 ppm NO$_3^-$−N^a	−0.9	H-cell	Carbon cloth	20.5	48.0	71
4	(Ba$_{0.5}$Sr$_{0.5}$)$_{0.85}$Co$_{0.8}$Fe$_{0.2}$O$_{3-\delta}$	0.5 M KNO$_3$ + 0.1 M K$_2$SO$_4$	−0.45	H-cell	Glassy carbon	8429.4	97.9	72
5	R-Co$_{0.8}$Fe$_{0.2}$O$_{3-\delta}$	0.1 M PBS + 0.1 M NaNO$_3$	−0.9	H-cell	Carbon cloth	1011.8	90.3	73
6	LaCoO$_3$	1 M Na$_2$SO$_4$ + 0.5 M KNO$_3$	−1.0	H-cell	Carbon cloth	4180.0	91.5	74
7	(La$_{0.2}$Pr$_{0.2}$Nd$_{0.2}$Ba$_{0.2}$Sr$_{0.2}$)CoO$_{3-\delta}$	0.05 M K$_2$SO$_4$ + 0.1 M KNO$_3$	−0.7	H-cell	Carbon cloth	129.0 (−0.9 V vs. RHE)	76.0	75
8	LaNd$_{0.25}$Pr$_{0.25}$Er$_{0.25}$Eu$_{0.25}$CuO$_4$	0.5 M K$_2$SO$_4$ + 500 ppm NO$_3^-$−N	−0.7	H-cell	Carbon cloth	81.1 (−1.0 V vs. RHE)	100.0	76
9	LaSrNiCoMnFeCuO$_3$	0.5 M K$_2$SO$_4$ + 500 ppm NO$_3^-$−N	−0.6	H-cell	Glassy carbon	97.5 (−0.9 V vs. RHE)	100.0	16
10	La$_{0.9}$FeO$_{3-\delta}$	0.1 M Na$_2$SO$_4$ + 0.1 M NaNO$_3$	−0.8	H-cell	Carbon cloth	60.3 (−1.0 V vs. RHE)	78.1	77
11	LaF$_{0.9}$R$_{0.1}$O$_3$	1 M KOH + 0.1 M KNO$_3$	−0.6	H-cell	Carbon cloth	980.0 (−0.8 V vs. RHE)	98.5	78

^{a} NO$_3^-$−N: the concentration of nitrogen in the form of nitrate, expressed as the mass of nitrogen.

perovskite (La$_{0.2}$Pr$_{0.2}$Nd$_{0.2}$Ba$_{0.2}$Sr$_{0.2}$)CoO$_{3-\delta}$, the synergistic effect of multiple A-site cations changes the crystal field environment, inducing Co to transition from a low-spin (LS) to a high-spin (HS) state, resulting in the re-distribution of electrons in the e_g and t_{2g} orbitals (Fig. 5a). Compared with the LS configuration (Fig. 5b), the Co active site in the HS state possesses more unpaired electrons in the partially filled 3d orbital, which facilitates charge transfer to the antibonding π^* orbital of NO$_3^-$, thereby enhancing its activation (Fig. 5c). The electrocatalytic performance for NH$_3$ generation is significantly enhanced, achieving a threefold increase in yield (129 mmol g$_{cat.}^{-1}$ h^{-1}) and a twofold increase in FE (76%) compared to LaCoO$_3$ under optimal potential. Online differential electrochemical mass spectrometry and DFT calculations confirmed that A-site high-entropy management effectively lowered the thermodynamic barrier of the rate-determining deoxygenation step (*HNO$_3$ + H$^+$ + e$^-$ → *NO$_2$ + H$_2$O), thus accelerating the overall NO$_3$RR process. Using electrospinning technology, Chen et al. constructed high-entropy La$_{0.9}$Sr$_{0.1}$Ni$_{0.2}$Co$_{0.2}$Mn$_{0.2}$Fe$_{0.2}$Cu$_{0.2}$O$_3$ (LaSrNiCoMnFeCuO$_3$) porous nanotubes and systematically investigated their formation mechanism under various calcination procedures (Fig. 5d).[16] They found that the differential diffusion of metal ions and the decomposition behavior of polymer templates during calcination were critical factors for nanotube structure formation. The material exhibited an impressive near-100% FE for NH$_3$ production. Structural and mechanistic analysis revealed that the strong interactions among multiple metal species within the high-entropy framework, along with the multi-site synergistic effects and a high density of unsaturated active sites, collaboratively optimized the electronic structure and surface charge distribution. These features enhanced the adsorption and activation of NO$_3^-$ ions and effectively lowered the energy barrier for the NO$_3$RR. Chen et al. adopted similar strategy and synthesis method to prepare LaNd$_{0.25}$Pr$_{0.25}$Er$_{0.25}$Eu$_{0.25}$CuO$_4$ (LNPEEC) high-entropy perovskite oxide nanotube (Fig. 5g) for NO$_3$RR, in which the FE of NH$_3$ reached 100% (Fig. 5h).[76] They found that the disordered arrangement of multi-rare earth elements at the A-site can regulate the d-band center of the B-site metal and optimize the adsorption strength of reactants and reaction intermediates (Fig. 5i).

Oxygen vacancies play a key role in NO$_3$RR, which enhance the adsorption and activation of reactant molecules and promote the transfer of electrons on the catalyst surface and the conversion of intermediates. Zheng et al. studied four kinds of perovskite oxides with different crystal structures, namely cubic LaCrO$_3$, orthorhombic LaMnO$_3$ and LaFeO$_3$, and hexagonal LaCoO$_3$.[74] XPS, electron paramagnetic resonance spectroscopy, and electrochemical measurements indicated that the oxygen vacancy amount and the NO$_3$RR catalytic activity follow the same sequence, i.e., LaCrO$_3$ < LaMnO$_3$ < LaFeO$_3$ < LaCoO$_3$, highlighting the great potential of oxygen-vacancy-rich perovskite oxides as catalysts for the efficient electrochemical synthesis of NH$_3$ via the NO$_3$RR. In another study, Chu et al. constructed a series of oxygen vacancy-rich perovskite oxide submicrofibers through the B-site substitution strategy.[71] Synchrotron-based X-ray absorption spectroscopy (XAS) reveals
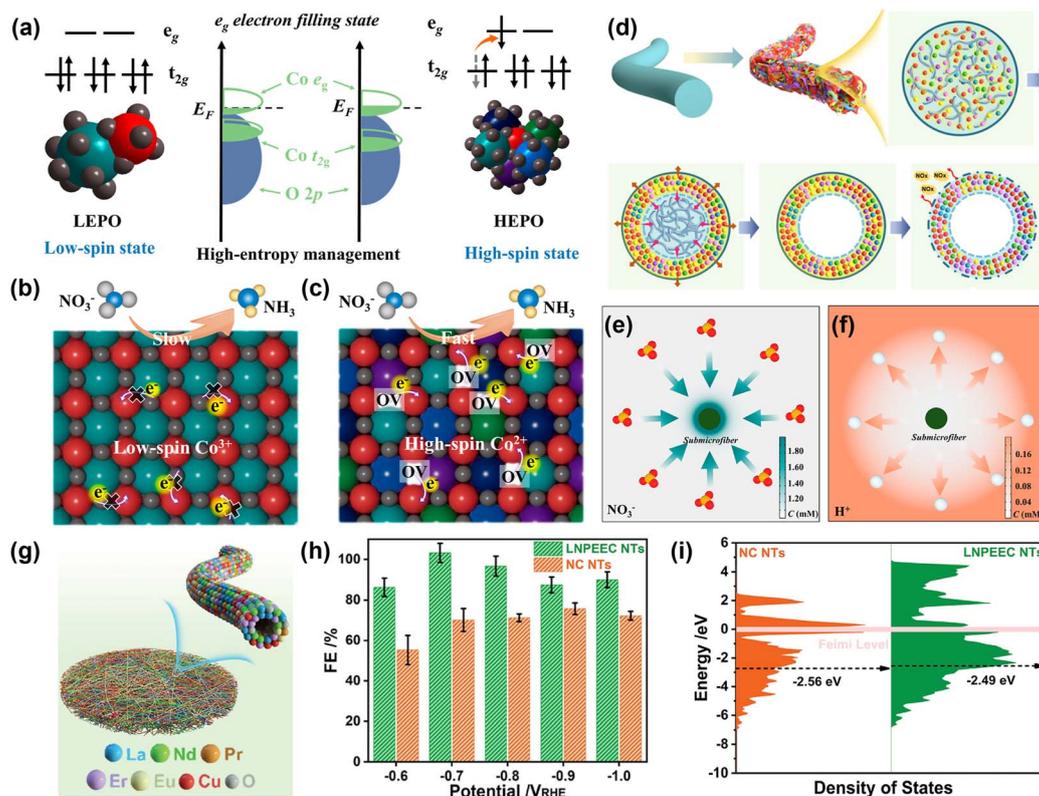
Fig. 5 Schematic diagram: (a) regulation of the Co spin state in perovskite through high-entropy control strategy; (b) slow NO₃RR process in low-entropy materials; and (c) fast NO₃RR process in high-entropy materials.[75] Copyright 2025, American Chemical Society. (d) Schematic illustration of the growth mechanism of LaSrNiCoMnFeCuO₃ porous nanotubes.[16] Copyright 2024, American Chemical Society. Top view of the model showing the variation of (e) NO₃⁻ and (f) H⁺ concentrations on the fiber surface.[71] Copyright 2023, American Chemical Society. (g) Schematic diagram of LNPEEC nanotubes and (h) corresponding FE for NH₃ production. (i) Electronic state density and d orbital center of copper in LNPEEC nanotubes and Nd₂CuO₄ nanotubes.[76] Copyright 2024, Wiley-VCH GmbH.

charge redistribution on $LaFe_{0.9}Cu_{0.1}O_{3-\delta}$ submicrofibers and confirms that the increase in Fe 3d–O 2p orbital hybridization favors the generation of surface oxygen vacancies. COMSOL Multiphysics simulation results showed that the cation substitution strategy can induce a more positive surface potential, thereby promoting more NO_3^- to be fixed on the catalyst surface and effectively inhibiting the hydrogen evolution reaction (HER) process (Fig. 5e and f). The above studies show that constructing specific crystal or geometric structures to expose accessible active sites of perovskite oxides can achieve efficient electrocatalytic processes.

3.3 Electrocatalytic nitrogen oxidation

NO_3^- is one of the important raw materials in the industrial and agricultural fields. The current industrial production of NO_3^- relies on two energy-intensive processes, the Haber–Bosch process (400–500 °C, 200–300 atm) and the Ostwald oxidation process (400–600 °C, 150–250 atm), resulting in tremendous energy consumption and carbon emission.[83–85] Electrocatalytic NOR can directly convert N_2 into NO_3^- under ambient conditions, providing a sustainable and environmentally friendly way to synthesize NO_3^-. In the field of NOR, research has primarily focused on the design of catalysts based on metal

nanomaterials, metal oxides and their composites.[86–89] Studies have shown that the cationic centers and adjacent oxygen vacancies in metal oxides can not only regulate the adsorption and activation of reactant molecules but also significantly influence the reaction kinetics.[89,90] As a class of metal oxides with tunable structures and compositions, perovskite oxides possess the ability to host multivalent cations and typically exhibit higher concentrations of oxygen vacancies compared to conventional metal oxides.[32,74] These features offer unique advantages for tuning catalytic activity and selectivity. Although perovskite oxides have demonstrated excellent performance in electrocatalytic CO₂RR, OER and other fields,[91–93] their application in NOR had remained unexplored until 2024. Recently, Zheng *et al.* demonstrated the feasibility of oxygen-vacancy-rich perovskite oxides ($Sr_{0.9}RuO_3$) for electrocatalytic NOR, opening a new avenue for the application of these materials in nitrogen fixation electrocatalysis (Fig. 6a).[7] By introducing A-site defects (*i.e.*, partial loss of Sr-sites), the formation of oxygen vacancies within the lattice was effectively promoted. Characterization results revealed that the oxygen vacancy concentration in $Sr_{0.9}RuO_3$ was significantly higher than in the $SrRuO_3$. The $Sr_{0.9}RuO_3$ perovskite oxide exhibited a high FE of 38.6% (Fig. 6b) and a NO_3^- yield rate of 17.9 mmol $g_{cat.}^{-1}$ h^{-1}. Theoretical analysis indicates that oxygen vacancy-rich $Sr_{0.9}RuO_3$ can
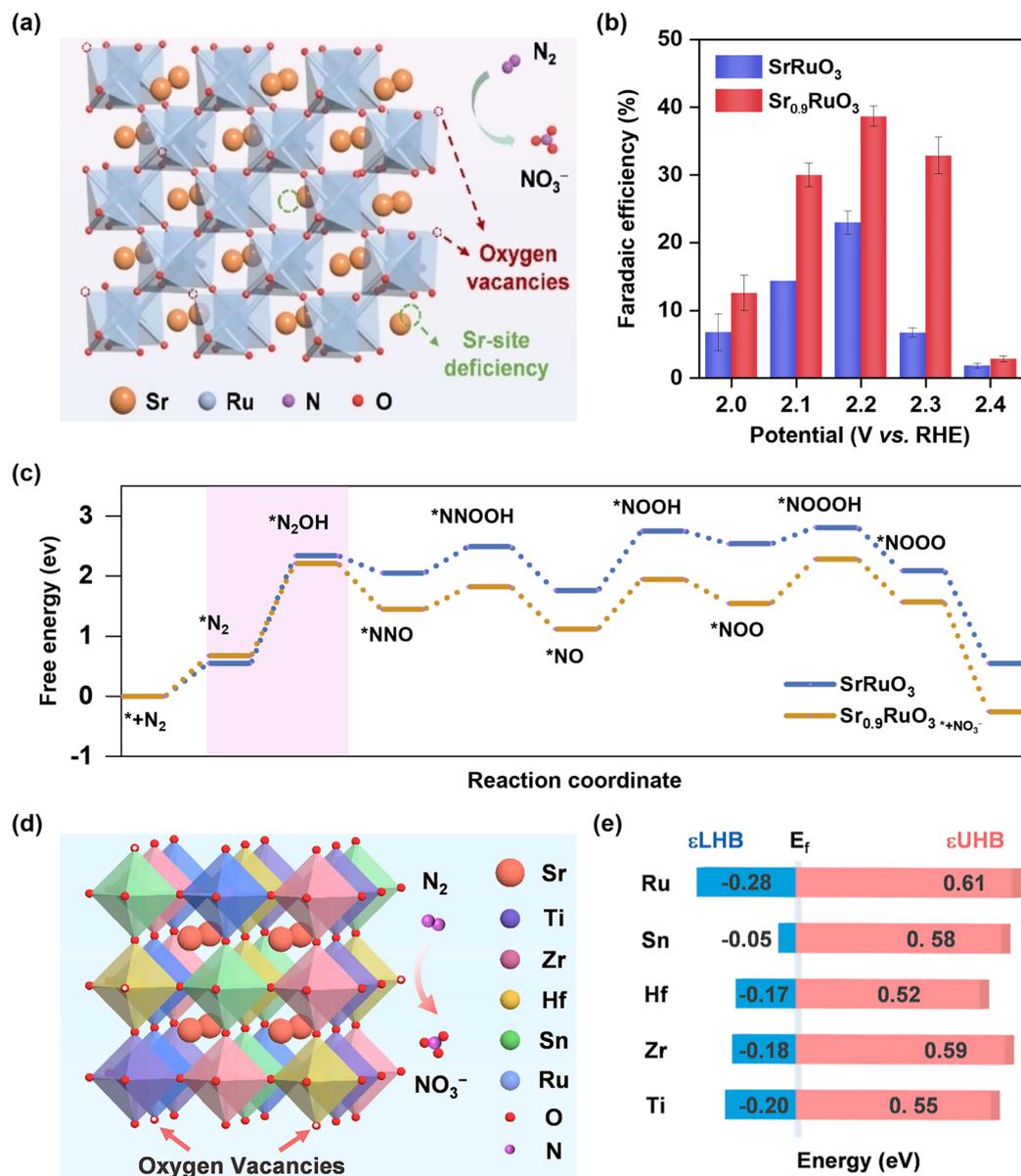
Fig. 6 (a) Schematic illustration of enhancing NOR performance by tuning the Sr content in Sr_xRuO_3 perovskite oxides; (b) comparison of FE between $Sr_{0.9}RuO_3$ and $SrRuO_3$ at different potentials; (c) DFT calculations of Sr_xRuO_3 with and without oxygen vacancies, highlighting the crucial role of oxygen vacancies in NOR activity.[7] Copyright 2023, Wiley-VCH GmbH. (d) Schematic representation of the high-entropy perovskite $Sr(TiZrHfSnRu)O_3$ for NOR; (e) relative positions of the d-band centers of Ru, Sn, Hf, Zr, and Ti with respect to the Fermi level (E_f), obtained from DOS analysis (the centers below and above E_f are denoted as εLHB and εUHB, respectively), used to identify the dominant adsorption-active sites.[94] Copyright 2024, American Chemical Society.

effectively enhance N_2 adsorption and reduce the thermodynamic barrier (Fig. 6c). This work establishes oxygen-vacancy-rich perovskite oxides as a promising platform for the rational design of efficient NOR catalysts, providing new strategies and theoretical insights for the development of advanced catalysts in artificial nitrogen fixation.

Section 3.2 discussed that employing high-entropy strategies to regulate the metal composition of perovskite oxides can enhance their NO_3RR activity. Similarly, recent studies have shown that high-entropy strategies can also be used to modulate the concentration and distribution of oxygen vacancies in perovskites, thereby improving their catalytic performance in

NOR. Zheng *et al.* studied $Sr(Ti–Zr–Hf–Sn–Ru)O_3$ as a high-entropy perovskite catalyst for NOR (Fig. 6d), which revealed that the oxygen vacancy concentration in the high-entropy perovskite was notably higher than that in low-entropy perovskite oxides, leading to improved N_2 adsorption and activation.[94] As a result, the NO_3^- yield of the high-entropy perovskite catalyst reached 53.1 mmol $g_{cat.}^{-1}$ h^{-1} with a FE of 32.8%, approximately doubling that of the low-entropy perovskite catalyst. Specifically, density of states analysis of the B-site metal atoms reveals that the Ru-site exhibits a higher Coulomb interaction value compared to the other four metals (Fig. 6e), making it the primary adsorption site. This suggests

that although the high-entropy strategy introduces a "cocktail effect" in catalytic performance, there still exists a dominant metal species that serves as the most favorable adsorption center in the multicomponent system. In summary, perovskite oxides hold great potential for NOR due to their tunable composition and structure. Strategies such as introducing A-site deficiencies or employing high-entropy designs can effectively regulate the concentration and distribution of oxygen vacancies, thereby enhancing N_2 adsorption and activation while improving both thermodynamic and kinetic aspects of the reaction. Notably, high-entropy perovskite catalysts not only benefit from the synergistic "cocktail effect" of multiple metal species but also exhibit dominant adsorption centers, enabling efficient and selective NOR catalysis. These insights offer new theoretical and design strategies for developing advanced electrocatalysts for artificial nitrogen fixation.

Overall, although studies have demonstrated that perovskite oxides can achieve high activity and selectivity in NOR by manipulating oxygen vacancies and transition metal sites, research in this area remains very limited. Currently reported work focuses primarily on a few systems and is insufficient to fully reveal the structure–performance relationship. Meanwhile, the NOR reaction often competes with the OER, posing pressing challenges in maintaining product selectivity and electrode stability at high current densities. Furthermore, quantitative detection methods for nitrate/nitrite products also have limitations, necessitating greater cross-validation using methods such as ion chromatography and isotope labeling. It is foreseeable that the development of more systematic material systems and reliable characterization methods will be key to advancing NOR research towards maturity.

4 Application of perovskite oxides in electrocatalytic carbon fixation

Electrocatalytic CO_2RR is a sustainable approach to convert the greenhouse gas CO_2 into value-added products such as CO, CH_4, formic acid, ethanol, and ethylene. The overall CO_2RR process involves CO_2 adsorption, activation (*e.g.*, bending of the linear molecule or weakening of the C=O bond), sequential proton–electron transfer steps, and eventual desorption of the desired products.[95] The involvement of multiple proton–electron transfer pathways leads to various products whose distribution mainly depends on the catalyst and reaction conditions.[96] Electron transfer between the catalyst surface and
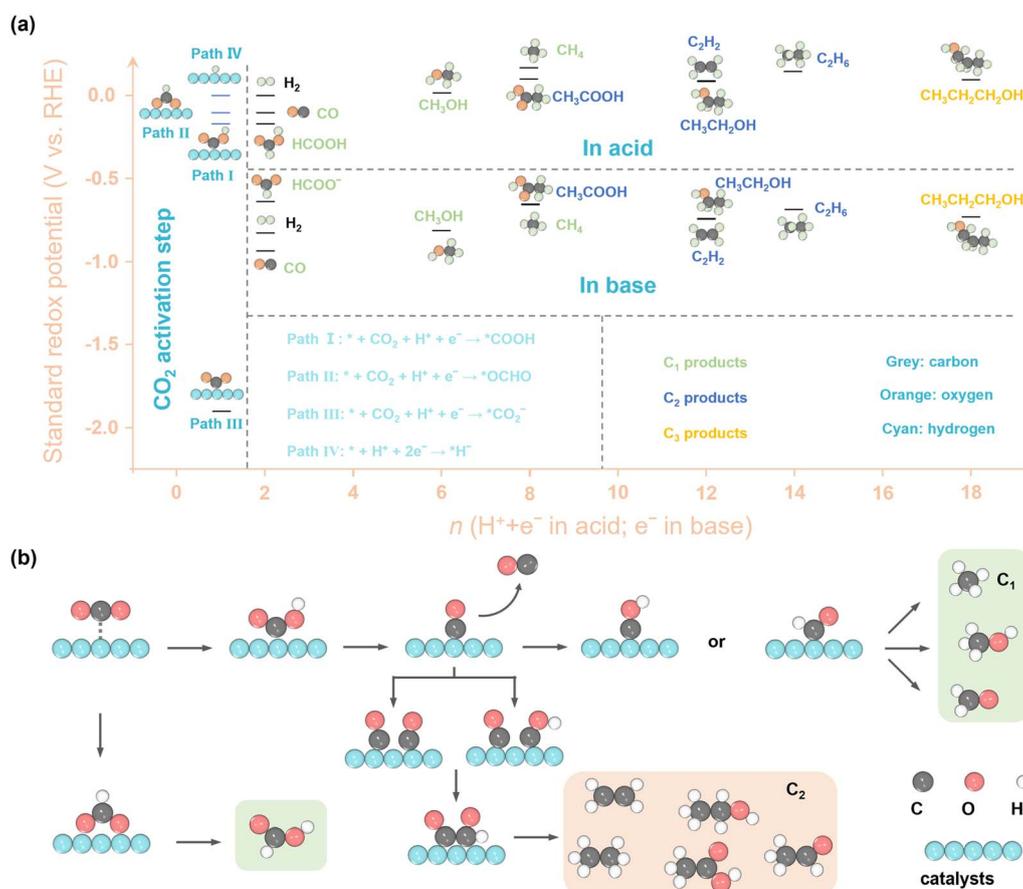

Fig. 7 CO_2RR thermodynamics and pathways. (a) Overview of the standard redox potential *versus* concerted proton–electron transfer or electrons for CO_2RR toward different products. (b) Reaction network highlighting key intermediates (*OOCH, *COOH, *CO, *CHO, *OCCO) that steer C_1 and C_2 formation; arrows denote elementary steps. CO is a central intermediate whose adsorption strength critically governs selectivity and catalyst stability considerations.

CO_2 intermediates plays a critical role, as it governs the change in oxidation state and the formation of specific products.[97]

As shown in Fig. 7a and b, in the electrochemical reduction of CO_2 to C_1 products, CO_2 first undergoes proton-electron coupling to form key intermediates, namely *OOCH or *COOH. The *OOCH intermediate is protonated and desorbs as formic acid ($HCOOH$), while *COOH is further hydrogenated to generate water and *CO.[98] The resulting *CO can be further transformed into intermediates, such as *CHO or *COH, and subsequently reduced to methanol (CH_3OH) or methane (CH_4) through multiple proton–electron transfer steps.[99] For the generation of C_2 products, the rate-determining step is C–C coupling, which typically occurs *via* *CO dimerization to form *OCCO, or *via* coupling between *CO and other intermediates such as *CHO or *CH.[100–102] *CO is recognized as a central intermediate in CO_2RR, and its adsorption strength on the catalyst surface plays a critical role in dictating the reaction pathway and product distribution. If *CO binds too weakly, it readily desorbs as CO; if too strongly, it may lead to catalyst deactivation.[103] Therefore, designing catalysts with an optimal *CO adsorption strength is crucial for promoting the formation of multi-carbon products.[104,105] Understanding the reaction pathway helps to reveal the generation and transformation process of different intermediates, providing a theoretical basis for optimizing the electronic structure of the catalyst and regulating the adsorption strength of key intermediates (such as *CO) to achieve precise control of product distribution. This is of great guiding significance for the development of highly selective and efficient CO_2RR catalysts.

Based on the above understanding of the CO_2RR reaction pathway and intermediate regulation mechanism, rational design of the composition and structure of perovskite oxide-based catalysts has become a key direction for improving the activity and selectivity of CO_2RR. To regulate the CO_2RR pathway to selectively generate C_1 products (such as formate, $HCOOH$ and CH_4), researchers have developed a variety of strategies. In terms of formate and $HCOOH$ products, Zhang *et al.* utilized microwave-assisted synthesis to incorporate La^{3+} ions into $BaSnO_3$, markedly enhancing the electrocatalytic performance for CO_2RR to formate.[106] Comprehensive characterizations revealed that La^{3+} substitution effectively modulated the Sn–O bond length, leading to local charge density enrichment. This structural modulation facilitated CO_2 adsorption and accelerated electron transfer kinetics, ultimately significantly improving the FE of formate. Chen *et al.* enhanced the conversion of CO_2 to $HCOOH$ on Sn-based perovskite oxides by tuning the Sn–O bond length through control of the A-site cation radius.[107] To verify this concept, a series of $Ba_{1-x}Sr_x$-SnO_3 ($x = 0, 0.25, 0.5, 0.75$ and 1) catalysts were synthesized as model systems with tunable Sn–O bond lengths. As the average A-site cation radius decreased from 1.61 Å to 1.44 Å, the Sn–O bond length shortened from 2.06 Å to 2.02 Å (Fig. 8a). As theoretically predicted, this shortening enhanced the Sn–O covalency and shifted the overall electronic band center closer to the E_f (Fig. 8b), thereby modulating the electronic structure of the material. Electrocatalytic performance tests revealed a volcano-type relationship between Sn–O bond length and both

the activity and selectivity for formic acid production. Among them, $Ba_{0.5}Sr_{0.5}SnO_3$ with an optimal Sn–O bond length of 2.04 Å showed the best performance, achieving a FE of 90.9% for $HCOOH$ at −1.2 V *vs.* RHE. Theoretical calculations further indicated that the improved performance originated from the advantages brought by the tuned electronic structure, including accelerated electron/proton transfer, optimized adsorption and activation of reaction intermediates, and a lowered energy barrier for *OCHO formation.

In terms of CH_4 product, Zhu *et al.* developed a rock-salt ordered Cu-based double perovskite oxide, Sr_2CuWO_6, as a proof-of-concept catalyst for the efficient and stable electro-reduction of CO_2 to CH_4.[108] At a current density of 400 mA cm^{-2}, the material achieved a FE of 73.1% for CH_4. Experimental results and theoretical calculations attribute this outstanding activity to two key factors: (1) a long Cu–Cu distance ($\geq$5.4 Å), which promotes the hydrogenation of *CO intermediates while suppressing C–C coupling; (2) a pronounced superexchange interaction, where O^{2-}-mediated electron transfer stabilizes the Cu-sites and prevents structural collapse during operation. Compared with a physical mixture of CuO and WO_3, Sr_2CuWO_6 exhibits up to a 14.1-fold enhancement in CH_4 production activity and selectivity, alongside significantly improves operational stability. This work introduces a novel design strategy for Cu-based CO_2RR catalysts by leveraging superexchange-stabilized, long-range active site configurations. In addition, Zhang *et al.* synthesized a series of $La_2CuO_4/(CaO)_x$ ($x = 0.2–1.2$) hybrid materials using La_2CuO_4 and CaO as building units, achieving enhanced efficiency and stability for CO_2 electro-reduction to CH_4 through precise control of interface size.[109] As the CaO content increased, the overall structure remained stable while the interface size gradually expanded. Benefiting from a one-pot self-assembly strategy, La_2CuO_4 and CaO formed tightly integrated interfaces, inducing significant electron transfer from Ca^{2+} to Cu^{2+} and generating strong interfacial coupling (Fig. 8c). Electrocatalytic tests revealed a volcano-type relationship between interface size and both the production rate and selectivity of CH_4, with the $x = 0.8$ sample exhibiting the best performance (Fig. 8d). Experimental and theoretical analyses indicated that the strong interfacial interaction facilitated *CO adsorption and hydrogenation, which promoted CH_4 formation, and also stabilized the Cu–O lattice, improving resistance to structural degradation.

As for CO_2RR to C_2 products, Li *et al.* developed a highly efficient CO_2RR catalyst by *in situ* socketing sub-3 nm Cu nanoparticles into a perovskite framework ($La_{0.4}Sr_{0.4}Ti_{0.9}O_{3-\delta}$), thereby constructing a system with strong metal-support inter-action (SMSI).[110] In this catalyst, ellipsoidal ultrasmall Cu particles are homogeneously and epitaxially anchored on the perovskite backbones, which not only modulates the electronic structure of Cu but also enhances the adsorption and activation of key intermediates while improving structural stability. Experimental results revealed that this catalyst significantly outperforms the physical mixture, achieving up to 6.2-fold enhancement in both C_2^+ product selectivity and catalytic activity, along with remarkable long-term operational stability exceeding 80 hours. Further, Chen *et al.* promoted the
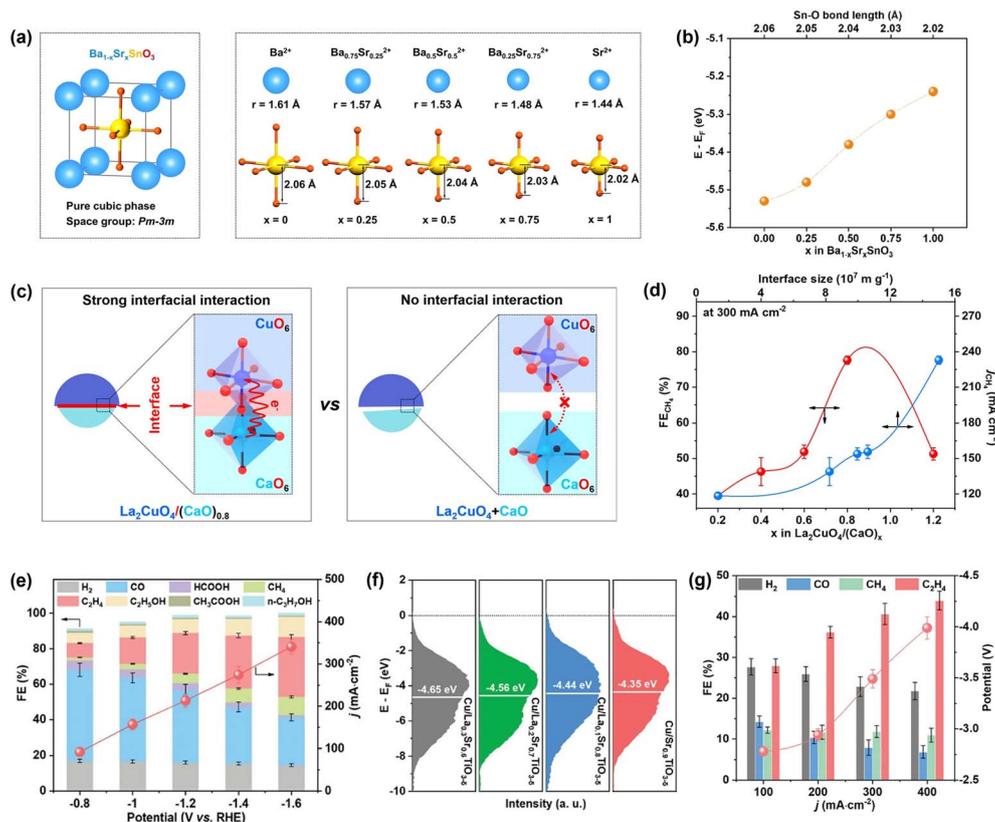
Fig. 8 (a) Crystal structure model of $Ba_{1-x}Sr_xSnO_3$ and the variation trend of Sn−O bond length with increasing Sr doping content.[107] Copyright 2023, Wiley-VCH GmbH. (b) Effect of the Sn−O bond length (or x value) on the total band center of $Ba_{1-x}Sr_xSnO_3$ series. (c) Schematic illustration of strong interfacial interaction in $La_2CuO_4/(CaO)_{0.8}$ (left) compared with the absence of interfacial coupling in the physical mixture of La_2CuO_4 and CaO (right).[109] Copyright 2024, American Chemical Society. (d) Correlation of FE_{CH4} or j_{CH4} with the x value and interface size at 300 mA cm^{-2} over the $La_2CuO_4/(CaO)_x$ series. (e) The effect of applied potentials on the product distribution and current density of CO_2RR over the Cu/$Sr_{0.9}TiO_{3-\delta}$ catalyst.[111] Copyright 2024, Wiley-VCH GmbH. (f) Valence band XPS spectra comparison of Cu/$La_{0.3-x}Sr_{0.6+x}TiO_{3-\delta}$ catalyst with different A-site cation valence states, demonstrating the obvious correlation between the total energy band center and the oxygen vacancy concentration. (g) In the MEA electrolyzer, the potentials of the Cu/$Sr_{0.9}TiO_{3-\delta}$ catalyst under different applied current densities and the corresponding FE of CO_2RR products were recorded, showing that the catalyst still has high activity and selectivity at high current density.

conversion of CO_2 to C_2^+ products on nano-socketed Cu/$La_{0.3-x}Sr_{0.6+x}TiO_{3-\delta}$ (x = 0, 0.1, 0.2, 0.3) perovskite heterostructures by modulating A-site valence states to control surface/interface oxygen vacancy concentrations.[111] As the A-site cation valence decreased from +2.1 to +1.8 (with x increasing from 0 to 0.3), the oxygen vacancy concentration significantly increased (from ∼15.6% to 28.0%). Flow cell tests showed a positive correlation between CO_2RR activity, C_2^+ product selectivity, and oxygen vacancy concentration. In particular, the Cu/$Sr_{0.9}TiO_{3-\delta}$ catalyst with the highest oxygen vacancy concentration showed strong suppression of the HER and delivered the best performance (Fig. 8e). Both experimental and theoretical results indicated that the oxygen vacancies modulated the electronic structure, shifting the overall band center closer to the E_f (Fig. 8f), which enhanced charge transfer, improved adsorption/activation of reactants, and lowered the energy barrier for C−C coupling. Furthermore, in a membrane electrode assembly (MEA) electrolyzer, Cu/$Sr_{0.9}TiO_{3-\delta}$ demonstrated high activity and selectivity for C_2H_4 production under industrial current densities with excellent stability (Fig. 8g).

In summary, perovskite oxides exhibit great potential in CO_2 electroreduction due to their tunable composition, excellent electronic structures, and strong metal–support interactions. Through rational structural design and doping modulation, they can effectively enhance the adsorption and conversion of key intermediates, significantly improve catalytic activity, product selectivity, and long-term stability, making them promising candidates for constructing efficient CO_2RR catalytic systems.

5 Electrocatalytic C−N coupling reaction

Perovskite oxides have demonstrated excellent performance in multiple electrocatalytic processes such as CO_2RR, OER, and NRR due to their unique crystal structure, abundant metal sites, and controllable electronic properties. Considering the complex requirements for the adsorption regulation of intermediates, electron transfer pathways, and the coordination of reaction sites in C−N coupling reactions, the unique programmability of

A/B-sites and interface regulation capabilities of perovskite oxides make them a promising C–N coupling catalytic platform. However, at present, only a few studies have initially explored the application of perovskite in C–N coupling.[92,112–114] Preliminary studies have shown that constructing dual-metal active centers (*e.g.*, Cu–Fe, Cu–Co) facilitates the separate activation and hydrogenation of CO_2 and nitrogen-containing species, respectively. Such cooperative sites can regulate intermediate adsorption configurations and electron transfer pathways, thus significantly reducing the energy barrier for C–N bond formation (Fig. 9a).[115–117] It's important to note that direct energetic evidence for this effect in perovskite systems is still lacking, so it's more appropriate to consider it as a plausible trend or hypothesis. However, studies in other catalyst types (such as metal–nitrogen–carbon materials and copper-based heterostructures)[118–121] have demonstrated that bimetallic sites can stabilize key intermediates and improve coupling efficiency, providing indirect support for this speculation. Further exploration is warranted by introducing M–O–M structures or oxygen vacancy-rich regions into the perovskite lattice. This may help stabilize intermediates such as *CO and *NH$_x$, potentially enhancing long-range electronic interactions through superexchange or bridge configurations (*e.g.*, Cu–O–Fe), thereby creating a more dynamic environment suitable for C–N coupling. Furthermore, the surface reconfiguration capabilities of perovskites and anion doping may also provide opportunities for the dynamic generation of new active sites. While these speculations lack direct experimental verification, they provide interesting avenues for future research. Kim *et al.* developed a fluorine-doped strontium ferrite ($SrFeO_{2.95-\delta}F_{0.05}$, SFF005) catalyst.[92] By regulating the F-doping ratio and using CO_2 to induce structural reconstruction, they prepared the reconstructed R-SFF005, which exhibited excellent performance in

the electrochemical synthesis of urea (Fig. 9b). This catalyst achieved a FE of 35.8% with a high urea yield of 34.7 mmol $g_{cat.}^{-1}$ h^{-1} in a H-cell and demonstrated good stability in multiple cycles. DFT calculations indicated that the center of the Fe d band after structural reconstruction shifted downward, which was conducive to C–N coupling and CO_2RR. This work highlights the crucial role of anion-doping induced surface reconstruction in enhancing the catalytic performance of perovskite oxides. Lv *et al.* systematically investigated the effect of doping concentration on urea electrosynthesis performance by constructing a series of Co-doped $SrRuO_3$ catalysts ($SrCo_x$-$Ru_{1-x}O_{3-\delta}$).[113] This study revealed that appropriate Co doping ($x = 0.39$) could introduce abundant oxygen vacancies, induce lattice strain, and significantly modulate the electronic structures of the Co- and Ru-sites (Fig. 9c and d), thereby promoting the formation of *CO and *NH$_2$ intermediates and facilitating C–N coupling. The optimized catalyst achieved a high urea yield of 25.3 mmol $g_{cat.}^{-1}$ h^{-1} and a FE of 34.1% at −0.7 V *vs.* RHE. Experimental and theoretical results demonstrated that the strain effect induced by doping broke the scaling relationship of adsorption energies, reduced the kinetic barrier for coupling, and suppressed the formation of undesired by-products. This work reveals a new mechanism in which dual Co–Ru active sites synergistically enhance selective C–N coupling and offers an important strategy for the design of efficient electrocatalysts for urea synthesis (Fig. 9e).

Currently, research on perovskite oxides in C–N coupling has been mainly limited to urea synthesis, and their use in forming more complex products such as amides or amines has not yet been reported. However, the structural tunability of perovskites, including flexible A/B-site composition, oxygen vacancy engineering, and dynamic surface reconstruction, suggests strong potential for expanding their catalytic scope. These
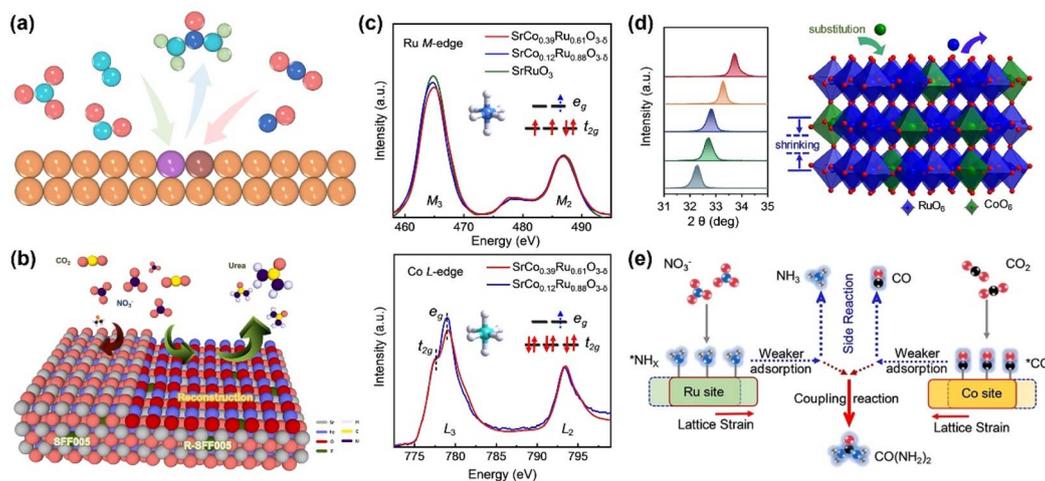

Fig. 9 (a) Schematic illustration of dual-site promoted C−N coupling, exemplified by urea synthesis. Cyan balls: nitrogen atoms. Light green balls: hydrogen atoms. Blue balls: carbon atoms. Red balls: oxygen atoms. Orange balls: catalyst substrate. Purple and brown: different doping metal sites. (b) Schematic diagram of urea synthesis using reconstructed fluorine-doped strontium ferrite metal oxide (SFF005).[92] Copyright 2024, Elsevier B.V. (c) XANES spectra of the Ru M-edge and Co L-edge for $SrRuO_3$, $SrCo_{0.12}Ru_{0.88}O_{3-\delta}$ and $SrCo_{0.39}Ru_{0.61}O_{3-\delta}$.[113] Copyright 2024, Wiley-VCH GmbH. (d) Enlarged XRD patterns of $SrCo_xRu_{1-x}O_{3-\delta}$ ($x = 0, 0.12, 0.24, 0.30, 0.39$, from bottom to top) and schematic of the strained Co−Ru dual-site crystal structure. (e) Schematic of the doping-engineering strategy for breaking the scaling relationship of intermediate adsorption.

characteristics could in principle stabilize key intermediates and enable multi-step coupling pathways beyond urea formation. Although experimental studies are still lacking, this unexplored area represents a promising direction for future research.

In conclusion, the research on perovskite oxides in C–N coupling reactions is still in its infancy, but the tunable structure, strong metal-carrier interaction, and multifunctional site construction capabilities of perovskite oxides offer rich possibilities for their applications. Future work can focus on: (1) precisely regulating the A/B-site elements to achieve electronic structure matching, (2) introducing synergistic sites (such as double centers or oxygen vacancies), and (3) combine *in situ* characterization with theoretical calculation to reveal the key steps and rate-limiting factors of C–N coupling. These directions are expected to promote the in-depth development of perovskite oxides in C–N coupling reactions and expand their application boundaries in green synthesis and the synergistic conversion of carbon and nitrogen resources.

6 Performance improvement strategies

Although perovskite oxides have attracted widespread attention due to their flexible structures and high electrocatalytic activity, their conductivity, active sites and intermediate adsorption capacity are still limited. Luckily, researchers have developed a variety of optimization strategies, inclusive of doping engineering, defect engineering, heterogeneous engineering and crystal face engineering, to improve their catalytic performance. This section will systematically summarize these four strategies, and explain their mechanism of action and application effects in combination with typical literature cases, providing theoretical support and practical paths for the rational design of perovskite oxide catalysts. It is worth noting that, due to the relatively limited studies on some of these optimization strategies in carbon and nitrogen fixation reactions, this part also draws on representative findings from other electrocatalytic systems to supplement the theoretical basis and broaden the design perspective.

6.1 Doping engineering

6.1.1 Anion doping. Anion doping, especially the use of non-metallic elements (such as F^-) to partially replace the O^{2-} in the perovskite oxygen site, is an effective strategy for electronic structure regulation.[30,122,123] The introduction of anions with different electronegativity or radius can weaken the Coulomb force between the B-site cation and oxygen anion, and change the local coordination environment, charge distribution and crystal field strength of the B-site transition metals.[124] Through theoretical and experimental studies, Li *et al.* employed an F^- substitution strategy to regulate the oxygen sites in $LaCoO_3$, constructing an F-substituted $LaCoO_3$ catalyst ($LCOF_{0.5}$) for efficient electrocatalytic NO_3RR.[124] The fundamental reason for the enhanced performance lies in the introduction of F^-, which weakens the hybridization between the O

2p and Co 3d orbitals, thereby generating more oxygen vacancies. These abundant oxygen vacancies further facilitate the electron transfer and surface adsorption of key intermediates during NO_3RR, significantly improving the catalytic activity. Notably, Ran *et al.* also observed remarkable performance improvement in the OER with F^- doped $LaCoO_3$.[122] Their mechanism emphasized that the high electronegativity of the F element strengthened the covalency of the metal–oxygen bond, regulated the spin state distribution of the Co^{3+} ions, and improved the electronic structure, thereby enhancing charge transport and catalytic efficiency (Fig. 10a). At first glance, this seems contradictory to Li *et al.*'s view of weakened hybridization. However, these two perspectives actually reflect the multidimensional effects of F^- on electronic structure regulation. Specifically, the localized weakening of hybridization favors oxygen vacancy formation and increases active sites, while enhanced covalency improves electronic conductivity and charge mobility. Although the regulatory focus of F^- doping varies with the reaction system, both cases underscore its effectiveness in enhancing the catalytic performance of perovskite oxides through anion engineering. This highlights a versatile strategy for the rational design of high-performance catalysts. Furthermore, moderate anion doping (such as F^-) can not only reduce the oxygen vacancy formation energy but also promote dynamic surface reconstruction, thereby generating a surface layer with higher activity. For example, Zhang *et al.* demonstrated that F doping in the $LaNi_{0.75}Fe_{0.25}O_3$ significantly enhances the surface reconstruction behavior and improves OER performance.[125] However, excessive doping may cause crystal structure destruction and reduced electronic conductivity, and a balance needs to be struck between activity enhancement and structural stability. In summary, anion doping effectively tailors the electronic structure and defect chemistry of perovskite oxides by inducing oxygen vacancies, enhancing adsorption and electron transfer of key intermediates, and promoting dynamic surface reconstruction. These effects synergistically improve catalytic activity and electronic conductivity. While doping levels must be carefully controlled to maintain structural integrity, anion doping has proven to be a powerful and versatile strategy for enhancing the catalytic performance of perovskite-based materials.

6.1.2 Cation doping. Perovskite oxide has good crystal structure tolerance, which can accept cations of various sizes and valence states. Introducing heterogeneous cations to regulate the crystal structure, electronic structure, defect concentration and adsorption behavior of reaction intermediates of the material is one of the core strategies for improving the electrocatalytic performance.[126,127] According to the doping site of perovskite oxide, cation doping can be divided into A-site cation doping and B-site cation doping. For B-site doping, Zhang *et al.* enhanced the NO_3RR performance of $LaCoO_3$ by doping it with different proportions of Mn.[128] Among them, the $LaMn_{0.6}Co_{0.4}O_3$ catalyst with the optimal doping ratio exhibited a 41.92% improvement in performance compared to the undoped $LaCoO_3$. This work also proposed that Mn doping not only regulates the valence state of Co but also activates adsorbed oxygen, acting as an electron donor participating in the
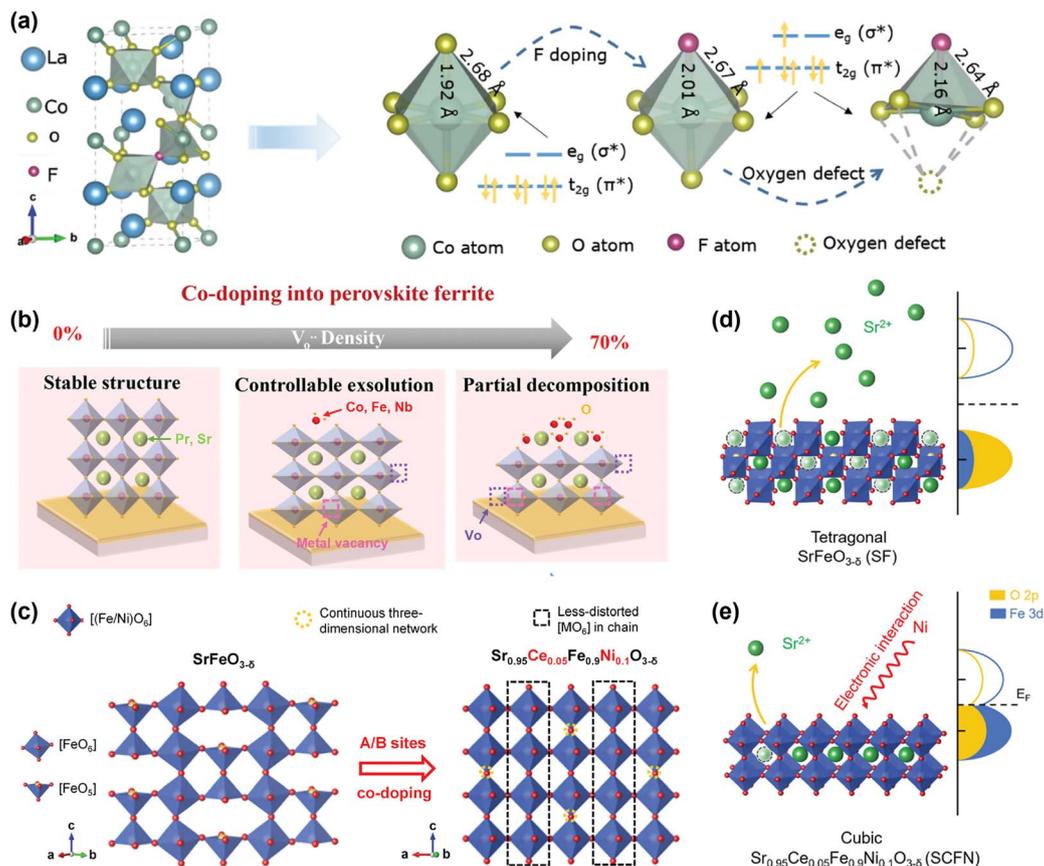
Fig. 10 (a) Schematic diagram of the mechanism of the influence of fluorine doping and oxygen vacancy synergistic regulation on the Co−O bond length and Co electron orbital occupancy (e_g/t_{2g}) in $LaCoO_3$ perovskite.[122] Copyright 2022, Wiley-VCH GmbH. (b) Schematic diagram of the evolution of crystal structure and the behavior of surface B-site cations after thermal reduction with the increase of Co doping in the B-site lattice.[29] Copyright 2021, Wiley-VCH GmbH. (c) Schematic diagram of the structural optimization path from SF to SCFN, showing the regulatory effect of Ce/Ni co-doping on the crystal structure integrity and three-dimensional skeleton stability.[131] Copyright 2021, Wiley-VCH GmbH. (d and e) Schematic diagram of Ce/Ni doping to inhibit Sr precipitation.

reaction to facilitate electron transfer, thereby overall enhancing the catalytic performance. Similarly, Li *et al.* constructed catalysts ($x = 0.025, 0.05, 0.1$) by lightly doping Cu^{2+} into inert $SrTiO_3$, which showed significantly improved CO_2RR activity and product selectivity compared to pristine $SrTiO_3$ and the physical mixture of $SrTiO_3$ and CuO.[129] Experimental characterizations revealed that the enhanced performance mainly stems from the introduction of stable CuO_6 octahedra, upshifted band center, accelerated charge transfer, and improved adsorption of reaction intermediates due to Cu^{2+} doping. In addition to modulating the valence state of active centers and promoting electron transfer, Chen *et al.* systematically revealed the effect of B-site Co doping level on the crystal structure stability and surface oxygen vacancy concentration of $Pr_{0.4}Sr_{0.6}Co_xFe_{0.9-x}Nb_{0.1}O_{3-\delta}$ films during the hydroxide oxidation reaction (Fig. 10b).[29] Experiments combined with DFT calculations indicate that the enhancement in catalytic performance originates from Co doping-induced weakening of the metal–O bonds, distortion of the FeO_5 octahedra, and reduction of oxygen vacancy formation energy. For A-site doping, Dong *et al.* partially substituted the A-site La^{3+} in RP-type La_2CuO_4 with Ag^+ to synthesize a series of

$La_{2-x}Ag_xCuO_{4-\delta}$ ($x = 0$–0.5) catalysts.[130] Among them, the $La_{1.8}Ag_{0.2}CuO_4$ catalyst achieved an FE of 86.4% for C_2 products, outperforming La_2CuO_4 (67%). Both experimental and theoretical results indicate that Ag doping introduces oxygen vacancies, modulates the crystal and electronic structures, facilitates electron transfer, shifts the d-band center closer to the Fermi level, enhances the adsorption of intermediates, and thereby improves the activity and selectivity of the CO_2RR.

6.1.3 Double doping. In recent years, an increasing number of researchers have focused on the synergistic enhancement effect brought about by double doping at the A/B and O sites. Double doping can simultaneously regulate the lattice structure, charge compensation and electronic band structure to selectively guide reaction paths in the catalytic process. The research of She *et al.* in OER shows that the A/B co-doping strategy in $Sr_{0.95}Ce_{0.05}Fe_{0.9}Ni_{0.1}O_{3-\delta}$ (SCFN) significantly improves the stability of the material by synergistically regulating the crystal structure and electronic structure (Fig. 10c).[131] The substitution of Ce^{3+} for Sr^{2+} makes the Goldschmidt tolerance factor closer to 1, which is conducive to the formation of cubic structure, enhances the three-dimensional connectivity of the crystal, and inhibits the leaching of alkaline earth metals

and structural collapse. Meanwhile, the introduction of Ni at the B-site enhances the electronic interaction between Ni–Fe and improves the metal–oxygen covalency, thereby inhibiting the surface amorphization phenomenon (Fig. 9d and e). Thus, compared with the original structure, SCFN exhibits better structural integrity and resistance to ion dissolution. This work also confirms the universality of this strategy in Fe-based parent perovskite oxides. Liu *et al.* proposed an innovative dual-site iodine doping strategy in the field of electrocatalytic OER, in which iodine cations and anions were doped into the B-site and oxygen vacancies of the $Ba_{0.5}Sr_{0.5}(Co_{0.8}Fe_{0.2})_{0.9}O_{3-\delta}$ perovskite, respectively.[132] This strategy effectively regulated the electronic configuration of the local B-site metal and oxygen site, enhanced the covalent mixing between the Co-site and the O anion, and thus improved the covalency of the transition metal–oxygen bond. The results show that the iodine-doped system exhibits a better Co cation e_g orbital occupancy number ($\sim$1.20) and abundant O_2^{2-}/O^- active species, which helps to improve the electron transfer efficiency and intrinsic activity of the material.

Although A/B-site doping strategy has been widely applied to enhance the electrocatalytic performance of perovskite, it still faces several key challenges: (1) doping stability: at strong reduction/oxidation potentials, doping ions may migrate or be lost, affecting the structural stability of the catalyst, (2) doping uniformity: excessive or uneven doping may lead to phase separation and the generation of impurity phases, affecting the consistency of activity, (3) complexity of doping mechanism: the electronic reconstruction and lattice distortion caused by doping are often difficult to be fully analyzed by traditional experimental methods and require in-depth research relying on means such as synchrotron radiation and *in situ* XAS. The future development direction should focus on multi-doping high-throughput screening and theory-experiment collaborative design, combining machine learning and DFT theory to calculate and predict the quantitative relationship among doping elements, doping ratio and performance. Meanwhile, the *in situ* characterization methods are utilized to analyze the evolution mechanism of doping active centers during the dynamic reaction process, which will provide a solid foundation for the transformation of perovskite oxides from laboratory research to industrial application.

6.2 Defect engineering

The strong structural tolerance of perovskite oxides renders them stable structures even after introducing a certain amount of cation or anion defects. Defect engineering is an effective strategy to improve the catalytic performance of perovskite oxides, involving cation vacancies and oxygen vacancies, which can induce local structural changes by regulating the component ratio, affecting the valence state and coordination environment of the B-site metal, thereby optimizing the electronic structure and reaction path.

6.2.1 Oxygen vacancy. Oxygen vacancy, as an important structural factor regulating the reactivity of perovskite oxides, has received great attention in the field of electrocatalysis in recent years. Oxygen vacancies can serve as adsorption sites for reaction intermediates, regulate charge transfer, and change electronic structure and surface potential distribution, affecting catalytic pathways and product selectivity.[133–136] Therefore, constructing and precisely regulating the oxygen vacancies in perovskite materials has become one of the core strategies to enhance their performance in electrocatalytic carbon fixation and nitrogen fixation. Ion substitution and the non-stoichiometric method are usually adopted for oxygen vacancy introduction.[127] Heterovalent substitution is often accompanied by changes in the metal valence state at the B-site and the generation of oxygen vacancies due to charge imbalance, while isovalent substitution promotes oxygen vacancy generation by causing lattice distortion and lowering the oxygen vacancy formation energy. Since both A-site and B-site cations are coordinated with oxygen, changes in either may induce the formation of oxygen vacancies. Besides, non-stoichiometric cations and oxygen anions can also induce oxygen vacancies. Among them, non-stoichiometric cations are relatively easy to achieve by simply regulating the ratio of precursors, while non-stoichiometric oxygen anions are more challenging to regulate due to several influencing factors, including structure, synthesis conditions and environment.[137] At present, accurately identifying the type and concentration of oxygen vacancies and establishing their association with structure and performance are still challenging. The key role of oxygen vacancies in improving the catalytic performance of perovskites has been widely confirmed. From the perspective of reaction mechanism, oxygen vacancies can act as electron-enriched centers to regulate the electronic structure of the transition metal B-site, thereby optimizing the adsorption and activation process of key intermediates.[133–135] In addition, the local lattice distortion and band structure regulation caused by oxygen vacancies can promote interfacial charge transfer, regulate the reaction path, and especially play an important role in selectivity control.[15,74] For instance, in the NOR process, the oxygen vacancy can lower the energy barrier for the oxidation of $*N_2$ to $*N_2OH$ (the NOR-determined rate step), promoting the formation of NO_3^- products.[7] During the reduction process of nitrogen-containing species such as NO_3^- or NO_2^-, oxygen vacancies help stabilize intermediates such as $*NO_2$ and $*NH_2$, enhancing the hydrogenation efficiency.[71,73]

The basis of this mechanism has also been verified by a large number of experiments. For instance, Nan *et al.* successfully introduced oxygen vacancies into $BiFeO_3$ perovskite (Vo-$BiFeO_3$) through reduction treatment, and Vo-$BiFeO_3$ was significantly better than the original $BiFeO_3$ in terms of NH_3 production rate and FE at various test potentials.[57] Oxygen vacancy filling experiments found that the NH_3 production rate and FE of the oxygen-treated catalyst (Vo-refilled-$BiFeO_3$) were significantly reduced, which further confirmed the key role of oxygen vacancies in improving NRR catalytic performance. Zheng *et al.* used a high-entropy strategy to perform multi-element doping on $SrRuO_3$, which induced the formation of high-density oxygen vacancies, thereby significantly enhancing its ability to selectively oxidize N_2 to NO_3^- and achieving a performance improvement twice that of the original catalyst in the NOR

reaction.[94] Similarly, Chu *et al.* reported a high-entropy perovskite material, $Ba_x(FeCoNiZrY)_{0.2}O_{3-\delta}$, with a lava-like morphology, as an electrocatalyst for the NRR.[138] By adjusting the non-stoichiometric ratio of A-site elements ($x = 0.9$ and 1.0), a higher density of oxygen vacancies was introduced, significantly enhancing both the NH_3 yield and selectivity. Specifically, the $Ba_{0.9}(FeCoNiZrY)_{0.2}O_{3-\delta}$ catalyst achieved 1.51 times the NH_3 yield and 1.95 times the FE compared to $Ba(FeCoNiZrY)_{0.2}O_{3-\delta}$.

Although oxygen vacancy engineering holds great promise in perovskite catalysis, several challenges remain: (1) a high concentration of oxygen vacancies may lead to structural instability or even irreversible reconstruction of the catalyst during the reaction; (2) current control over the concentration, spatial distribution, and dynamic behavior of oxygen vacancies remains limited; (3) conventional characterization techniques struggle to distinguish surface and bulk vacancies or track their dynamic evolution;[143] (4) oxygen vacancies often interact with factors like metal valence and charge distribution, making it difficult to isolate their effects. In the future, combining advanced *in situ* techniques with theoretical simulations will be key to understanding vacancy behavior and constructing stable, well-controlled vacancy structures for precise performance tuning.

6.2.2 Cation defect.
Cation defect, as an important type of spot defects, also demonstrates unique regulatory capabilities in electrocatalytic reactions. The regulation of A-site cation vacancies has been proven to be an important means to activate

the lattice oxygen on the surface of perovskite and reconstruct the electronic structure. Yang *et al.* proposed a novel polarity reversal strategy to induce *in situ* etching of $LaFeO_3$ (LFO-PI), thereby introducing La and O vacancies (Fig. 11c).[139] Compared with the original $LaFeO_3$ (LFO-Pri), LFO-PI showed a 5.2-fold performance improvement in NO_3^--N removal. The enhancement was mainly attributed to the increase in surface potential and the upward shift of the d-band center caused by polarity regulation, which synergistically promoted the adsorption and enrichment of NO_3^- on the catalytic surface, thereby accelerating the NO_3RR process. Similarly, Li *et al.* constructed a p-type $SrFeO_{3-\delta}$ perovskite (SFO-Srv) containing Sr vacancies by chemical etching in the CO oxidation reaction, successfully activated its lattice oxygen to form a highly covalent $Fe^{(4-x)+}$–$O^{(2-x)-}$ active site (Fig. 11d).[140] The study confirmed for the first time that this highly covalent site can dynamically consume and regenerate holes during the reaction, realizing a hole-mediated reversible redox process of lattice oxygen. This hole-involved electronic regulation mechanism enhances the lattice oxygen cycling characteristic of the Mars–van Krevelen pathway. Further analysis indicates that the process is jointly influenced by Fe–O covalency, O 2p vacancy states, and the electron density of the Fe-site. Benefiting from the mechanism, SFO-Srv exhibits excellent activity and stability in CO oxidation reaction, demonstrating the universality of oxygen vacancy engineering. This study reveals the action mechanism of lattice oxygen in the catalytic oxidation process, and provides new ideas for the design of efficient metal oxide catalysts. Zhu *et al.*
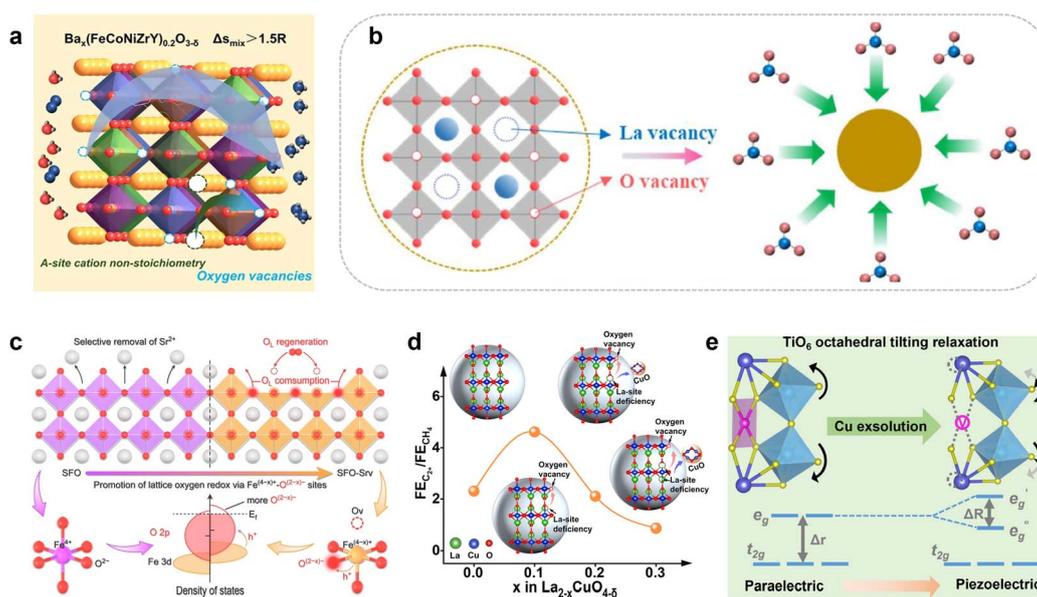

Fig. 11 (a) Schematic crystal structure of the high-entropy perovskite $Ba_x(FeCoNiZrY)_{0.2}O_{3-\delta}$, illustrating the introduction of oxygen vacancies *via* A-site cation non-stoichiometry and the disordered distribution of multiple transition metals at the B-site.[138] Copyright 2022, Springer Nature. (b) Schematic diagram of the synergistic regulation of catalytic performance by La vacancy and oxygen vacancy to promote the efficient electroreduction of NO_3^-.[139] Copyright 2026, Elsevier Ltd. (c) Schematic illustration of surface lattice oxygen redox behavior and the associated electronic structure modulation induced by the introduction of Sr vacancies in $SrFeO_{3-\delta}$ (from pristine SFO to SFO-Srv).[140] Copyright 2025, Wiley-VCH GmbH. (d) Schematic diagram of the structural evolution and catalytic behavior of $La_{2-x}CuO_{4-\delta}$ as the La-site defects increase.[141] Copyright 2021, Wiley-VCH GmbH. (e) Schematic illustration showing that the introduction of Cu defects in $CaCu_3Ti_4O_{12}$ leads to the tilting and relaxation of TiO_6 octahedra, atomic displacements around the defect sites, and crystal field splitting.[142] Copyright 2025, American Chemical Society.

systematically studied the influence of the defect of the A-site cation on Cu-based RP-type perovskite in the CO_2RR, confirming that this strategy can effectively optimize the catalytic performance.[141] After introducing the La-site defect, stable oxygen vacancies were induced, and a CuO/RP hybrid structure was also kept at a high defect level. The results show that with the increase of La defects, the activity and selectivity of CO_2RR products present a volcanic distribution: the sample with moderate La defect ($L_{1.9}C$) was optimal for the C_{2+} production, while the sample with CuO enrichment ($L_{1.7}C$) preferred for CH_4 formation (Fig. 11e). This product distribution difference was attributed to the synergistic effect of cationic defect and hybrid structure on the adsorption, activation and reaction pathway regulation of the key intermediate. These studies indicate that the A-site cation vacancies contribute to regulating the surface electronic structure and the configuration of active sites, and also serve as a key factor in activating lattice oxygen to participate in catalytic processes, demonstrating wide applicability in various reaction systems.

In addition to the regulation of A-site defects, the cation defect at the B-site is also a potential structural regulation method. Although their application in electrochemical carbon/nitrogen conversion remains limited, they have been explored in other electrochemical systems (such as solid oxide fuel cells) and photocatalysis, providing valuable insights for their further development in electrocatalytic applications.[142,144,145] For instance, Kuai et al. proposed that introducing a small amount of B-site cation vacancies (such as $Ba(Co_{0.4}Fe_{0.4}Zr_{0.1}Y_{0.1})_{0.975}O_{3-\delta}$ and $Ba(Co_{0.4}Fe_{0.4}Zr_{0.1}Y_{0.1})_{0.95}O_{3-\delta}$) into the $BaCo_{0.4}Fe_{0.4}Zr_{0.1}Y_{0.1}O_{3-\delta}$ perovskite can significantly enhance its ORR activity while maintaining the perovskite structure.[145] The introduction of vacancies helps lower the ORR activation energy, improving its potential for application in intermediate-to low-temperature solid oxide fuel cells. However, the defect concentration must be carefully controlled to avoid the formation of impurity phases that would increase charge transfer resistance. Wang et al. introduced Cu vacancies in $CaCu_3Ti_4O_{12}$ through a thermally driven selective dissolution strategy, revealing the feasibility of regulating piezoelectric properties with B-site defects (Fig. 11f).[142] Cu defects break the original framework stability of TiO_6 octahedron, inducing structural relaxation and local symmetry breaking, thereby endowing the material with significant polarization behavior and piezoelectric response. In practical applications, this defect engineering significantly enhances the piezoelectric photocatalytic performance, achieving efficient charge separation and active species generation. This work indicates that the B-site defect could regulate crystal symmetry and local polarization, providing new ideas for performance optimization in fields such as electrocatalysis. In summary, defect engineering provides an effective means to regulate the structure and surface properties of perovskite oxides. By precisely introducing cation or anion defects, the electronic structure, local crystal field and surface reaction environment can be significantly adjusted, thereby enhancing the selective adsorption and activation efficiency of reaction intermediates, and inducing new reaction pathways to achieve an essential improvement in electrocatalytic performance. In fact, multiple

defect types often exist in synergy. For example, A/B-site doping is often accompanied by oxygen vacancies. This synergistic effect is particularly critical for constructing efficient catalytic centers. At the same time, a deep understanding of defect formation and action mechanisms will help reveal the structure–performance relationship of perovskites in complex reaction processes. Therefore, the systematic development of defect regulation strategies will lay a solid foundation for the design of highly active and highly stable perovskite oxide electrocatalysts.

6.3 Heterostructure construction

Perovskite oxides can achieve significant enhancements in catalytic performance through the construction of heterostructures with other catalytic materials. The charge redistribution and lattice strain at the heterogeneous interfaces effectively modulate the electronic structure of the material, thereby facilitating catalytic reactions.[146] Moreover, heterostructures provide increased density of active sites and improved adsorption properties for reaction intermediates, leading to enhanced overall catalytic efficiency.[147,148] This section focuses on the design strategies of perovskite oxide-based hybrid heterostructures and their electrocatalytic performance.

Zhu et al. reported a nano-socketed $Cu/La_{0.3-x}Sr_{0.6+x}TiO_{3-\delta}$ heterostructure catalyst (Fig. 12a), where SMSI was engineered to effectively steer the product distribution in CO_2RR, demonstrating excellent capability for generating C_2^+ products.[111] The Cu nanoparticles are socketed within the perovskite framework, forming a synergistic interface that modulates the physico-chemical properties of the perovskite support, potentially enhancing electron transfer and providing auxiliary adsorption sites for reaction intermediates, further strengthening the interfacial effect and facilitating C–C bond formation. This work demonstrates the potential of heterogeneous structure design and carrier regulation to synergistically improve electrocatalytic performance, and provides new ideas for the construction of efficient C_2^+ product catalysts. Based on this, it is expected that more precise control of catalyst active sites and reaction intermediates can be achieved by further regulating the dissolution of metals and the metal-carrier interactions. Xu and his collaborators combined Ni exsolution with the metallic interaction of Pd to in situ construct PdNi nanocrystals on $La_{0.52}Ca_{0.28}Ni_{0.06}Ti_{0.94}O_3$ perovskite for NO_3RR (Fig. 12b).[149] The deposition of Pd not only improves the reducibility of the support and promotes the generation of oxygen vacancies, but also acts as a nucleation center for Ni exsolution, inducing the formation of PdNi bimetallic nanoparticles. Calculation results show that oxygen vacancies contribute to the adsorption of NO_3^-, while PdNi alloys regulate the interaction between NO_3^- and catalysts, enhance the adsorption of intermediates, and effectively inhibit the occurrence of HER. Sun's team systematically studied the catalytic performance of a series of perovskite thin film platforms ($La_{0.4}Ca_{0.4}Ti_{0.94}Ni_{0.06}O_3$, LCTN) modified with exsolution heterogeneous nanoparticles (Ni and NiO) in high-temperature CO_2RR and quantitatively analyzed their activities (Fig. 12c).[17] They found that the boundary length of the interface between the nanoparticles and the perovskite is
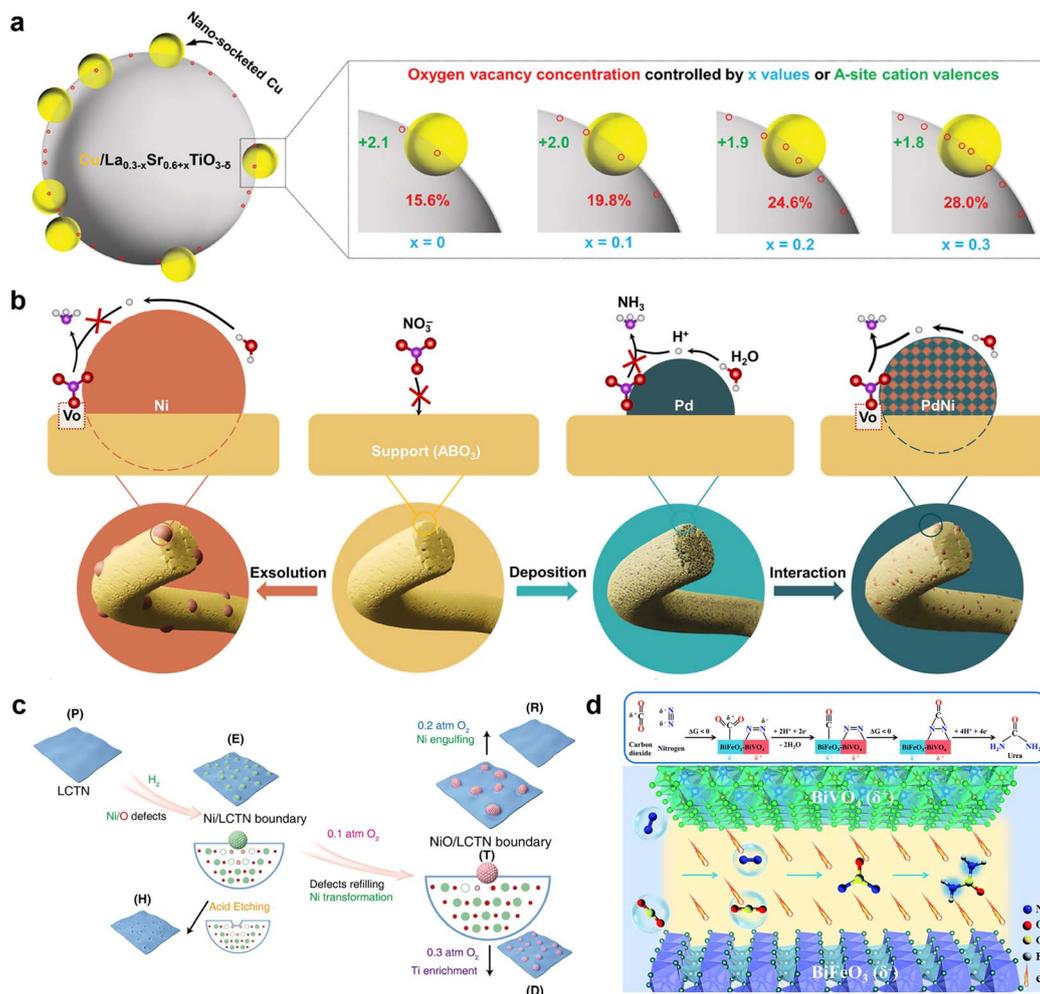
Fig. 12 (a) Schematic diagram of nano-socketed Cu/perovskite heterostructure and the relationship between surface oxygen vacancy concentration and the variation of x value in $Cu/La_{0.3-x}Sr_{0.6+x}TiO_{3-\delta}$ or the valence state of A-site cations.[111] Copyright 2024, Wiley-VCH GmbH. (b) Design of perovskite fiber catalyst loaded with alloy metal nanoparticles and schematic diagram of surface NO_3RR.[149] Copyright 2025, Elsevier B.V. (c) Schematic diagram of the construction of CO_2RR catalytic platform with various heterogeneous boundaries.[17] Copyright 2025, American Chemical Society. (d) Schematic diagram of the electrocatalytic urea synthesis mechanism based on the synergistic effect of $BiFeO_3/BiVO_4$ p–n heterostructure.[114] Copyright 2021, Royal Society of Chemistry.

strictly correlated with the CO_2RR activity. Among them, the NiO/LCTN heterogeneous interface plays a key role in stabilizing the oxidized carbon intermediates, increasing the onset potential of the formation of coupled carbon species, and inhibiting carbon accumulation. At the same time, p–n heterojunctions provide new kinetic advantages for multielectron coupling reactions. Yuan *et al.* used the p-type $BiFeO_3$ and n-type semiconductor $BiVO_4$ of perovskite structure to prepare a new p–n heterojunction electrocatalyst, which realizes the spontaneous electron transfer at the heterojunction interface through the built-in electric field (Fig. 12d).[114] The prepared perovskite structure $BiFeO_3/BiVO_4$ shows high electrocatalytic activity for the synthesis of urea by C–N coupling reaction.

6.4 Crystal surface engineering

In carbon/nitrogen fixation electrocatalytic reactions such as CO_2RR, NRR and NO_3RR, typically involve multistep proton–electron transfer and complex intermediates (such as *CO,

*NO_2, *NH_x, *etc.*). The adsorption selectivity and stability of these intermediates can be strongly influenced by the exposed crystal facets, which in turn determine the reaction rates and product distribution.[65,150,151] Perovskite oxides have good structural tunability and rich interfacial chemistry, which provides a broad space for their crystal surface engineering. In the fields of OER and solar cells, their crystal surface engineering effectively adjusts the configuration of active sites, optimizes the electronic structure and intermediate adsorption behavior of active sites, thereby significantly improving the catalytic efficiency.[152–154] However, compared to these fields, the application of crystal surface engineering in perovskite-based carbon- and nitrogen-fixation reactions remains limited. A clear structure–activity relationship between specific crystal facets and reaction mechanisms has yet to be established. Therefore, in the future, it is urgently necessary to introduce crystal face engineering into the catalytic system of perovskite oxides in carbon/nitrogen fixation reactions, combine crystal

face preferential growth, *in situ* characterization technology and theoretical simulation methods, and explore the regulatory mechanism of high-index crystal faces or exposed specific active sites on reaction pathways and product distribution, so as to provide new strategies and theoretical support for the development of efficient and highly selective perovskite catalysts.

In summary, the rational design strategies discussed above, including doping engineering, defect regulation, facet exposure, and heterostructure construction, have greatly improved the intrinsic activity, selectivity, and stability of perovskite oxide catalysts in laboratory-scale studies. Nevertheless, most studies remain limited to small electrodes or half-cell testing. The compatibility and performance retention of perovskites in MEAs or flow electrolyzers, which are closer to industrial conditions, remain to be verified, but are crucial for achieving industrially relevant performance. Furthermore, electrolyzer structural design is a key issue. Optimizing mass transfer, ion migration, and electrode–electrolyte interfacial processes is crucial for achieving stable and efficient conversion at high current densities. Moreover, ensuring long-term durability under continuous operation, especially at high current densities where structural reconstruction, dissolution, or phase transformation may occur, remains an open question. Another critical issue is scalability: the synthesis of perovskites with well-controlled structures (such as defect-rich architectures or high-entropy compositions) is often demonstrated only at small scale, whereas practical deployment requires reproducible, cost-effective, and environmentally friendly routes for larger-scale fabrication. These considerations highlight that, beyond material-level optimization, future research must also focus on device integration, operational stability, and system-level design to truly bridge the gap between laboratory discoveries and real-world applications.

7 Product detection methods

In the study of electrocatalytic nitrogen and carbon fixation reactions, the accuracy and reliability of product detection methods are crucial for evaluating catalyst performance. Different reaction systems often correspond to different target products, necessitating the selection of appropriate detection methods. However, many current studies overly rely on a single method, which can lead to biased results and even a lack of comparability between different studies. Therefore, systematically summarizing product detection methods and emphasizing their reliability is crucial for advancing research in this field. For NRR and NO_3RR, NH_3 is the core product. The most common detection method is UV-visible absorption spectroscopy, based on a chemical colorimetric reaction. This method is simple to operate and highly sensitive, but is susceptible to interference from external nitrogen sources and byproducts, resulting in quantitative errors. Ion chromatography (IC) can effectively distinguish various nitrogen-containing species, such as NH_4^+ and NO_2^-, with higher accuracy, but it requires strict experimental conditions and instrumentation. Furthermore, nuclear magnetic resonance (NMR) is also used for the qualitative and quantitative determination of ammonia, and is

particularly suitable for detecting organic nitrogen compounds. Notably, isotope labeling (such as $^{15}N_2$ or $^{15}NO_3^-$) is widely considered the "gold standard" for confirming product origin, avoiding interference from ambient nitrogen. For NOR, typical products are NO_3^- and NO_2^-. Common detection methods also include colorimetric UV-visible absorption spectroscopy and IC. The former is particularly sensitive for detecting NO_2^- but is susceptible to interference from coexisting species; the latter can accurately distinguish and quantify NO_3^- and NO_2^-, thus offering advantages in terms of reliability. In recent years, some studies have also combined ^{15}N isotope labeling to track the reaction process, further helping to confirm the true source of nitrogen oxidation products. For CO_2RR, the products are complex, including CO, formic acid, methanol, ethylene, and others. Gaseous products are typically detected using gas chromatography in combination with a thermal conductivity detector, flame ionization detector or mass spectrometry, enabling qualitative and quantitative analysis of multiple gaseous components. Liquid products are primarily detected using high-performance liquid chromatography (HPLC), IC or NMR. Small molecules such as formic acid and alcohols are susceptible to background signal interference at low concentrations, so cross-validation using multiple detection methods is recommended. Detection challenges are even greater for C–N coupling reactions (such as urea synthesis). Traditional urea detection relies on the diacetyl monoxime reaction combined with UV-visible absorption spectroscopy, which is simple to perform but can be subject to interference from byproducts (NO_2^- or NH_3) in complex reaction systems. HPLC can effectively distinguish urea from other nitrogen-containing species, improving quantitative accuracy. NMR offers unique advantages in confirming molecular structure, and combining it with ^{15}N isotope labeling can significantly enhance the confidence of detection results.

In summary, the accuracy of product detection is closely related to the method selected. Methods such as UV-visible absorption spectroscopy, IC, and NMR spectroscopy each have advantages and limitations. When used alone, errors are often difficult to completely avoid. Future research should prioritize standardization of assays and cross-validation using multiple methods, incorporating isotope labeling when necessary to ensure the reliability of results and comparability across studies.

8 Challenges and outlook

This review focuses on the application of perovskite oxides in electrocatalytic carbon/nitrogen fixation reactions, and systematically sorts out the research progress in major reactions including CO_2RR, NRR, NOR and NO_3RR. By summarizing the mainstream regulation strategies such as A/B-site doping, oxygen vacancy engineering, crystal plane regulation and heterostructure construction, we explain how these methods affect the electronic structure and catalytic behavior of perovskites, thereby optimizing product selectivity and reaction kinetics. In addition, we also discuss the exploration of perovskite catalysts in cutting-edge directions such as C–N coupling,

and conducted a preliminary discussion on the relationship between their structure and performance from the perspectives of material design and reaction mechanisms, providing theoretical references and strategic guidance for the future development of efficient catalysts.

Although perovskite oxides show broad application prospects in electrocatalytic carbon/nitrogen fixation reactions, they still face many challenges in further performance enhancement and mechanism revelations. First, the reaction system is complex and multiple pathways coexist. Especially in the synergistic reduction system of CO_2 and NO_3^-, there are many kinds of intermediate and intertwined reaction routes but without clear identifications of rate-limiting steps and true active centers. Second, perovskites are prone to structural reconstruction, surface dissolution or element migration during the electrolysis process, which affects their electrocatalytic stability. While oxygen vacancies can enhance the adsorption and activation of intermediates to a certain extent, excessive concentrations can induce local structural instability and even lead to irreversible lattice reconstruction. However, existing in situ and quasi in situ characterization techniques are still insufficient to comprehensively and real-time monitor these dynamic changes, limiting the in-depth understanding of the mechanisms behind stability degradation. Third, perovskite oxide catalysts generally exhibit insufficient electrical conductivity and slow charge transfer, making it difficult to adapt to industrial-grade reaction conditions such as high current density. Fourth, most of the current performance improvement strategies still rely on experience-driven, and a widely applicable structure–activity prediction system has not yet been established, which restricts the efficient screening and rapid development of new perovskite materials.

Looking ahead, the application of perovskite oxides in electrocatalytic carbon/nitrogen fixation reactions still has broad room for development. A deep understanding of related reaction mechanisms is the key to promoting the rational design of materials. It is urgent to use in situ characterization technology and theoretical simulation to reveal the evolution of active sites and the transformation process of intermediates under real electrolysis conditions, as well as build a closed-loop system of structure–performance-mechanism. Also, the development of interface-controllable heterostructures, the construction of dual active centers and multifunctional synergistic systems will further improve the selectivity of reaction pathways and product accuracy, especially for complex systems such as C–N coupling and CO_2RR/NO_3RR. In addition, the rich structural freedom of perovskites provides a good platform for machine learning and high-throughput computing, thus it is expected to achieve a paradigm shift from experimental-driven to prediction-driven catalyst screening. Finally, promoting the integrated application of perovskites in engineering systems, such as neutral electrolyte conditions which resemble natural aqueous environments and benefit perovskite structural stability and HER suppression, high current density and membrane electrodes, will provide solid support for the construction of efficient, green and sustainable carbon–nitrogen conversion technologies. In general, as a functional electrocatalytic material, perovskite oxide has the advantages of broad design space and strong structure–performance coupling, and is an important material platform for the future development of green synthetic fuels and nitrogen-based chemicals. With the continuous advancement of characterization methods and material design concepts, it is expected to move from "usable" to "optimal" in the field of electrocatalytic carbon/nitrogen fixation, providing key technical support for achieving carbon-nitrogen cycles and sustainable development goals.

Author contributions

All of the authors contributed to the literature search, writing and editing of this review.

Conflicts of interest

There are no conflicts to declare.

Data availability

No primary research results, software, or code have been included, and no new data were generated or analysed as part of this review.

Acknowledgements

Notes and references

1 S. Zhang, Y. Liu, Y. Ding, H. Wu, L. Qing, J. Zhu, S. Chen, Z. Wang, L. Zhang and T. Liu, Adv. Mater., 2025, 37, 2418681.

2 Y. Gong, P. Yang, J. Chen, J. Zhong and D. Ma, Compos. Commun., 2024, 51, 102109.

3 H. Li, N. Zhang, S. Bai, L. Zhang, F. Lai, Y. Chen, X. Zhu and T. Liu, Chem. Mater., 2022, 34, 7995.

4 Y. Zhang, H. Zheng, K. Zhou, J. Ye, K. Chu, Z. Zhou, L. Zhang and T. Liu, Adv. Mater., 2023, 35, 2209855.

5 Y. Ding, S. Zhang, S. Liu, Y. Liu, H. Zheng, L. Qing, Y. Song, Z. Ma, L. Zhang and T. Liu, Adv. Funct. Mater., 2025, 35, 2422339.

6 Y. Wang, Y. Kang, Y. Miao, M. Jia, S. Long, L. Diao, L. Zhang, D. Li and G. Wu, Compos. Commun., 2024, 45, 101789.

7 H. Zheng, Z. Ma, Y. Liu, Y. Zhang, J. Ye, E. Debroye, L. Zhang, T. Liu and Y. Xie, Angew. Chem., Int. Ed., 2024, 63, e202316097.

8 G. Chao, W. Zong, J. Zhu, H. Wang, K. Chu, H. Guo, J. Wang, Y. Dai, X. Gao, L. Liu, F. Guo, I. Parkin, W. Luo, P. Shearing, L. Zhang, G. He and T. Liu, J. Am. Chem. Soc., 2025, 147, 21432.

9 Z. Zhi, X. Fan, X. Tian, J. Niu, T. Sun, D. Li, L. Zhang and D. Yang, Compos. Commun., 2025, 57, 102452.

10 Z. Ma, S. Zhan, Y. Xie, Y. Liu, Y. Ding, S. Zhang, H. Lin, L. Zhang, T. Liu and Y. Xie, *Adv. Mater.*, 2025, **37**, 2420565.

11 P. Mhase, V. Pujari, S. Jadhav, A. Al-Sehemi, S. Alsobaie and S. Patange, *Compos. Commun.*, 2025, **54**, 102284.

12 Y. Wang, L. Wang, K. Zhang, J. Xu, Q. Wu, Z. Xie, W. An, X. Liang and X. Zou, *Chin. J. Catal.*, 2023, **50**, 109–125.

13 H. Sun, X. Xu, G. Chen and Z. Shao, *Carbon Energy*, 2024, **6**, e595.

14 M. Christy, S. Choi, J. Kwon, J. Jeong, U. Paik and T. Song, *Small Sci.*, 2025, **5**, 2400386.

15 K. Chu, F. Liu, J. Zhu, H. Fu, H. Zhu, Y. Zhu, Y. Zhang, F. Lai and T. Liu, *Adv. Energy Mater.*, 2021, **11**, 2003799.

16 Y. Chen, C. Chen, W. Huang, C. Pao, C. Chang, T. Mao, J. Wang, H. Fu, F. Lai, N. Zhang and T. Liu, *ACS Nano*, 2024, **18**, 20530–20540.

17 X. Zhang, X. Xiao, Q. Zhang, Z. Chen, C. Jiang, M. Chen, N. Yan, S. Mo, M. Wu, J. Li, J. Huang, A. Alodhayb, X. Fu, M. Chen, X. Lv and Y. Sun, *J. Am. Chem. Soc.*, 2025, **147**, 462–472.

18 Y. Li, N. Mushtaq, Y. Chen, W. Ye, Z. Zhuang, M. Singh, Y. Jing and L. Fan, *Adv. Funct. Mater.*, 2025, **35**, 2411025.

19 C. Yao, W. Liu, H. Zhang, H. Wang, W. Zhang, X. Lang and K. Cai, *Appl. Catal., B*, 2025, **363**, 124789.

20 J. Baek, Y. Kim, J. Ahn, D. Kim, H. Shin, J. Ko, S. Park, C. Park, E. Shin, J. Jang and I. Kim, *J. Mater. Chem. A*, 2022, **10**, 23282–23293.

21 P. Tan, M. Liu, Z. Shao and M. Ni, *Adv. Energy Mater.*, 2017, **7**, 1602674.

22 J. Hwang, R. Rao, L. Giordano, Y. Katayama, Y. Yu and Y. Shao-Horn, *Science*, 2017, **358**, 751–756.

23 W. Yin, B. Weng, J. Ge, Q. Sun, Z. Li and Y. Yan, *Energy Environ. Sci.*, 2019, **12**, 442–462.

24 X. Li, H. Zhao, J. Liang, Y. Luo, G. Chen, X. Shi, S. Lu, S. Gao, J. Hu, Q. Liu and X. Sun, *J. Mater. Chem. A*, 2021, **9**, 6650.

25 F. Li, D. Lin, Z. Chen, Z. Cheng, J. Wang, C. Li, Z. Xu, Q. Huang, X. Liao, L. Chen, T. R. Shrout and S. Zhang, *Nat. Mater.*, 2018, **17**, 349–354.

26 M. Zhang, G. Jeerh, P. Zou, R. Lan, M. Wang, H. Wang and S. Tao, *Mater. Today*, 2021, **49**, 351–377.

27 N. Ramadass, *Mater. Sci. Eng.*, 1978, **36**, 231–239.

28 M. Risch, *Catalysts*, 2017, **7**, 154.

29 H. Chen, C. Lim, M. Zhou, Z. He, X. Sun, X. Li, Y. Ye, T. Tan, H. Zhang, C. Yang, J. W. Han and Y. Chen, *Adv. Sci.*, 2021, **8**, 2102713.

30 C. Yang, Y. Tian, C. Yang, G. Kim, J. Pu and B. Chi, *Adv. Sci.*, 2023, **10**, 2304224.

31 H. Xie, Y. Zhang, P. Liu, X. Duo, Z. Hu, J. Yu, Z. Wang, G. Yao, L. Feng, X. Huang, R. Ouyang and Y. Wang, *Small*, 2024, **20**, 2400668.

32 Q. Ji, L. Bi, J. Zhang, H. Cao and X. Zhao, *Energy Environ. Sci.*, 2020, **13**, 1408–1428.

33 K. Wang, C. Han, Z. Shao, J. Qiu, S. Wang and S. Liu, *Adv. Funct. Mater.*, 2021, **31**, 2102089.

34 G. Fu, R. Hou, L. Sun, H. Liu, Y. Wei, R. Wei, X. Meng, S. Zhang and B. Yang, *ACS Appl. Mater. Interfaces*, 2025, **17**, 7860–7869.

35 M. Chen, Y. Zhang, F. Liu, Z. Zhang, Y. Dong, Y. Zhu, H. Jiang and J. Zhu, *Nano Res.*, 2024, **17**, 4682–4686.

36 Z. Wang, S. Han, Y. Zhang, X. Wang, Q. Bai and Y. Wang, *Renewable Energy*, 2024, **233**, 121180.

37 X. Liang, W. Yan, Y. Yu, K. Zhang, W. An, H. Chen, Y. Zou, X. Zhao and X. Zou, *Angew. Chem., Int. Ed.*, 2023, **62**, e202311606.

38 A. Grimaud, O. Diaz-Morales, B. Han, W. Hong, Y. Lee, L. Giordano, K. Stoerzinger, M. Koper and Y. Shao-Horn, *Nat. Chem.*, 2017, **9**, 457–465.

39 Y. Jiang, P. Wang, Y. Xiong, T. Chen, C. Zhang, K. Gao, X. Duan and D. Wang, *J. Mater. Chem. A*, 2023, **11**, 26707–26715.

40 J. Hwang, Z. Feng, N. Charles, X. Wang, D. Lee, K. Stoerzinger, S. Muy, R. Rao, D. Lee, R. Jacobs, D. Morgan and Y. Shao-Horn, *Mater. Today*, 2019, **31**, 100–118.

41 T. Han, S. Ma, X. Xu, P. Cao, W. Liu, X. Xu and S. Pei, *J. Alloys Compd.*, 2021, **876**, 160211.

42 Y. Song, S. Zhang, Y. Liu, Y. Ding, Z. Ma, Y. Liu, W. Fan and L. Zhang, *Compos. Commun.*, 2025, **55**, 102326.

43 S. Zhang, Y. Song, Y. Liu, J. Zhu, Z. Ma, L. Qing, Z. Wang, L. Zhang, T. Liu and Y. Xie, *Adv. Funct. Mater.*, 2025, e02874.

44 J. Mu, Z. Zhao, X. Gao, Z. Liu, W. Luo, Z. Sun, Q. Gu and F. Li, *Adv. Energy Mater.*, 2024, **14**, 2303558.

45 Z. Feng, G. Li, X. Wang, C. Gómez-García, J. Xin, H. Ma, H. Pang and K. Gao, *Chem. Eng. J.*, 2022, **445**, 136797.

46 C. Lv, N. Jia, Y. Qian, S. Wang, X. Wang, W. Yu, C. Liu, H. Pan, Q. Zhu, J. Xu, X. Tao, K. P. Loh, C. Xue and Q. Yan, *Small*, 2023, **19**, 2205959.

47 P. Guo, F. Yin, Z. Ni, L. Shi and G. Kofie, *Chem. Eng. J.*, 2025, **503**, 158390.

48 X. Yang, S. Sun, L. Meng, K. Li, S. Mukherjee, X. Chen, J. Lv, S. Liang, H. Zang, L. Yan and G. Wu, *Appl. Catal., B*, 2021, **285**, 119794.

49 S. Chen and J. Guan, *Chin. J. Catal.*, 2024, **66**, 20–52.

50 T. Ye, S. Park, Y. Lu, J. Li, J. Wu, M. Sasase, M. Kitano and H. Hosono, *J. Am. Chem. Soc.*, 2021, **143**, 12857–12866.

51 X. Cui, C. Tang and Q. Zhang, *Adv. Energy Mater.*, 2018, **8**, 1800369.

52 Y. Gao, M. Zhu, X. Liu, G. Dai, Y. Zhou, Z. Meng, L. Luo, T. Gan, F. Chen, Y. Zhou, W. Deng and S. Liu, *Chem. Eng. J.*, 2024, **493**, 152659.

53 C. Xue, X. Zhou, X. Li, N. Yang, X. Xin, Y. Wang, W. Zhang, J. Wu, W. Liu and F. Huo, *Adv. Sci.*, 2022, **9**, 2104183.

54 M. Ohrelius, H. Guo, H. Xian, G. Yu, A. A. Alshehri, K. Alzahrani, T. Li and M. Andersson, *ChemCatChem*, 2020, **12**, 731–735.

55 T. Zhang, Q. Wang, Y. Sun, J. Li and G. Liu, *Green Energy Environ.*, 2025, **10**, 1543–1550.

56 C. Li, D. Ma, S. Mou, Y. Luo, B. Ma, S. Lu, G. Cui, Q. Li, Q. Liu and X. Sun, *J. Energy Chem.*, 2020, **50**, 402–408.

57 J. Nan, Y. Fang, K. Rong, Y. Liu and S. Dong, *Appl. Catal., B*, 2024, **357**, 124328.

58 Y. Xu, X. Xu, N. Cao, X. Wang, X. Liu, M. Fronzi and L. Bi, *Int. J. Hydrogen Energy*, 2021, **46**, 10293–10302.

59 X. Hu, Y. Sun, S. Guo, J. Sun, Y. Fu, S. Chen, S. Zhang and J. Zhu, *Appl. Catal., B*, 2021, **280**, 119419.

60 S. Bastia, Y. Moses, N. Kumar, R. Mishra and Y. Chaudhary, *ACS Appl. Mater. Interfaces*, 2023, **15**, 13052–13063.

61 Y. Liu, X. Kong, X. Guo, Q. Li, J. Ke, R. Wang, Q. Li, Z. Geng and J. Zeng, *ACS Catal.*, 2020, **10**, 1077–1085.

62 S. Zhang, G. Duan, L. Qiao, Y. Tang, Y. Chen, Y. Sun, P. Wan and S. Zhang, *Ind. Eng. Chem. Res.*, 2019, **58**, 8935–8939.

63 G. Chao, J. Wang, W. Zong, W. Fan, T. Xue, L. Zhang and T. Liu, *Nanotechnology*, 2024, **35**, 432001.

64 J. Wang, G. Chao, W. Zong, K. Chu, J. Zhu, R. Chen, Y. Zheng, L. Zhang and T. Liu, *Chem. Eng. J.*, 2024, **499**, 156343.

65 L. Zheng, Y. Zhang, W. Chen, X. Xu, R. Zhang, X. Ren, X. Liu, W. Wang, J. Qi, G. Wang, C. Ma, L. Xu, P. Han, Q. He, D. Ma, J. Wang, C. Ling, D. Su, M. Shao and Y. Chen, *Angew. Chem., Int. Ed.*, 2025, **64**, e202500985.

66 L. Sun, C. Dai, T. Wang, X. Jin, Z. Xu and X. Wang, *Angew. Chem., Int. Ed.*, 2024, **63**, e202320027.

67 H. Lin, J. Wei, Y. Guo, Y. Li, X. Lu, C. Zhou, S. Liu and Y. Li, *Adv. Funct. Mater.*, 2024, **34**, 2409696.

68 S. Liu, W. Miao, K. Ma, H. Teng, X. Zhang, J. Li, W. Li, X. Cui and L. Jiang, *Appl. Catal., B*, 2024, **350**, 123919.

69 X. Liu, H. Liu, Y. Gao, X. Deng, Y. Hua, W. Sun, C. Li and J. Bai, *Int. J. Hydrogen Energy*, 2025, **105**, 382–388.

70 L. Yang, M. Liao, Z. Lin, J. Pan, W. Li, S. Lv and H. Cheng, *Sci. Adv.*, 2024, **348**, 127781.

71 K. Chu, W. Zong, G. Xue, H. Guo, J. Qin, H. Zhu, N. Zhang, Z. Tian, H. Dong, Y. Miao, M. J. Roeffaers, J. Hofkens, F. Lai and T. Liu, *J. Am. Chem. Soc.*, 2023, **145**, 21387–21396.

72 F. Liu, Z. Zhang, L. Shi, Y. Zhang, X. Qiu, Y. Dong, H. Jiang, Y. Zhu and J. Zhu, *J. Mater. Chem. A*, 2023, **11**, 10596–10604.

73 P. Hu, X. Zhang, M. Xu, Y. Lv, H. Guo, J. Chen, X. Ye, H. Xian, X. Sun and T. Li, *Appl. Catal., B*, 2024, **357**, 124267.

74 H. Zheng, Y. Zhang, Y. Wang, Z. Wu, F. Lai, G. Chao, N. Zhang, L. Zhang and T. Liu, *Small*, 2023, **19**, 2205625.

75 H. Guo, Y. Zhou, K. Chu, X. Cao, J. Qin, N. Zhang, M. B. J. Roeffaers, R. Zbořil, J. Hofkens, K. Müllen, F. Lai and T. Liu, *J. Am. Chem. Soc.*, 2025, **147**, 3119–3128.

76 C. Chen, Z. Xu, G. Hai, W. Huang, C. Pao, H. Li, K. Jiang, N. Zhang and T. Liu, *Small*, 2025, **21**, 2407964.

77 Q. Yin, S. Hu, J. Liu and H. Zhou, *Sustainable Energy Fuels*, 2022, **6**, 4716–4725.

78 M. Xia, C. Zhao, H. Xiao, W. Liu, Y. Li, H. Li, H. Ou and G. Yang, *ACS Catal.*, 2024, **14**, 12152–12162.

79 Y. Chida, T. Tomimori, T. Ebata, N. Taguchi, T. Ioroi, K. Hayashi, N. Todoroki and T. Wadayama, *Nat. Commun.*, 2023, **14**, 4492.

80 H. Li, Y. Han, H. Zhao, W. Qi, D. Zhang, Y. Yu, W. Cai, S. Li, J. Lai, B. Huang and L. Wang, *Nat. Commun.*, 2020, **11**, 5437.

81 H. Cai, H. Yang, S. He, D. Wan, Y. Kong, D. Li, X. Jiang, X. Zhang, Q. Hu and C. He, *Angew. Chem., Int. Ed.*, 2025, **64**, e202423765.

82 L. Xiao, Z. Wang and J. Guan, *Chem. Sci.*, 2023, **14**, 12850–12868.

83 Y. Wang, T. Li, Y. Yu and B. Zhang, *Angew. Chem., Int. Ed.*, 2022, **61**, e202115409.

84 Z. Nie, L. Zhang, X. Ding, M. Cong, F. Xu, L. Ma, M. Guo, M. Li and L. Zhang, *Adv. Mater.*, 2022, **34**, 2108180.

85 T. Li, S. Han, C. Cheng, Y. Wang, X. Du, Y. Yu and B. Zhang, *Angew. Chem., Int. Ed.*, 2022, **61**, e202204541.

86 H. Mao, Y. Sun, H. Li, S. Wu, D. Liu, H. Li, S. Li and T. Ma, *Adv. Mater.*, 2024, **36**, 2313155.

87 Y. Guo, S. Zhang, R. Zhang, D. Wang, D. Zhu, X. Wang, D. Xiao, N. Li, Y. Zhao, Z. Huang, W. Xu, S. Chen, L. Song, J. Fan, Q. Chen and C. Zhi, *ACS Nano*, 2022, **16**, 655–663.

88 H. Guo, Z. Guo, K. Chu, W. Zong, H. Zhu, L. Zhang, C. Liu, T. Liu, J. Hofkens and F. Lai, *Adv. Funct. Mater.*, 2023, **33**, 2308229.

89 M. Kuang, Y. Wang, W. Fang, H. Tan, M. Chen, J. Yao, C. Liu, J. Xu, K. Zhou and Q. Yan, *Adv. Mater.*, 2020, **32**, 2002189.

90 L. Zhang, M. Cong, X. Ding, Y. Jin, F. Xu, Y. Wang, L. Chen and L. Zhang, *Angew. Chem., Int. Ed.*, 2020, **59**, 10888–10893.

91 M. Humayun, Z. Li, M. Israr, A. Khan, W. Luo, C. Wang and Z. Shao, *Chem. Rev.*, 2025, **125**, 3165–3241.

92 H. Kim, T. J. Lim, H. Eom, Y. Kim, K. Kim and J. Lee, *Appl. Catal., B*, 2025, **365**, 124974.

93 U. Draz, E. Di Bartolomeo, A. Panunzi, U. Pasqual Laverdura, N. Lisi, R. Chierchia and L. Duranti, *ACS Appl. Mater. Interfaces*, 2024, **16**, 8842–8852.

94 H. Zheng, Y. Liu, Z. Ma, E. Debroye, J. Ye, L. Zhang and T. Liu, *ACS Nano*, 2024, **18**, 17642–17650.

95 J. Han, X. Bai, X. Xu, X. Bai, A. Husile, S. Zhang, L. Qi and J. Guan, *Chem. Sci.*, 2024, **15**, 7870–7907.

96 Z. Kou, X. Li, T. Wang, Y. Ma, W. Zang, G. Nie and J. Wang, *Electrochem. Energy Rev.*, 2022, **5**, 82–111.

97 Y. Wu, S. Cao, J. Hou, Z. Li, B. Zhang, P. Zhai, Y. Zhang and L. Sun, *Adv. Energy Mater.*, 2020, **10**, 2000588.

98 R. Kortlever, J. Shen, K. Schouten, F. Calle-Vallejo and M. Koper, *J. Phys. Chem. Lett.*, 2015, **6**, 4073–4082.

99 D. Gao, R. Arán-Ais, H. Jeon and B. Roldan Cuenya, *Nat. Catal.*, 2019, **2**, 198–210.

100 C. Wang, Z. Lv, Y. Liu, L. Dai, R. Liu, C. Sun, W. Liu, X. Feng, W. Yang and B. Wang, *Angew. Chem., Int. Ed.*, 2024, **63**, e202411216.

101 L. Fan, C. Xia, F. Yang, J. Wang, H. Wang and Y. Lu, *Sci. Adv.*, 2020, **6**, eaay3111.

102 Z. Du, S. Li, G. Liang, Y. Xie, Y. A, Y. Zhang, H. Zhang, J. Tian, S. Zheng, Q. Zheng, Z. Chen, W. Ip, J. Liu and J. Li, *J. Am. Chem. Soc.*, 2024, **146**, 32870–32879.

103 H. Cui, F. Yang, C. Liu, H. Zhu, M. Liu and R. Guo, *Small*, 2025, **21**, 2502867.

104 C. Zhan, F. Dattila, C. Rettenmaier, A. Bergmann, S. Kühl, R. García-Muelas, N. López and B. R. Cuenya, *ACS Catal.*, 2021, **11**, 7694–7701.

105 X. Liu, J. Xiao, H. Peng, X. Hong, K. Chan and J. Nørskov, *Nat. Commun.*, 2017, **8**, 15438.

106 Q. Zhang, S. Gao, Y. Yan, M. Li, W. Yan, Y. Huang and J. Cao, *ACS Appl. Mater. Interfaces*, 2025, **17**, 16881–16891.

107 M. Chen, K. Chang, Y. Zhang, Z. Zhang, Y. Dong, X. Qiu, H. Jiang, Y. Zhu and J. Zhu, *Angew. Chem., Int. Ed.*, 2023, **62**, e202305530.

108 J. Zhu, Y. Zhang, Z. Chen, Z. Zhang, X. Tian, M. Huang, X. Bai, X. Wang, Y. Zhu and H. Jiang, *Nat. Commun.*, 2024, **15**, 1565.

109 Y. Zhang, Y. Xu, Z. Chen, Z. Zhang, X. Liu, Z. Xue, X. Tian, X. Bai, X. Wang, M. Huang, J. Zhu, H. Jiang and Y. Zhu, *ACS Nano*, 2024, **18**, 31466–31477.

110 Y. Li, F. Liu, Z. Chen, L. Shi, Z. Zhang, Y. Gong, Y. Zhang, X. Tian, Y. Zhang, X. Qiu, X. Ding, X. Bai, H. Jiang, Y. Zhu and J. Zhu, *Adv. Mater.*, 2022, **34**, 2206002.

111 M. Chen, Y. Xu, Y. Zhang, Z. Zhang, X. Li, Q. Wang, M. Huang, W. Fang, Y. Zhang, H. Jiang, Y. Zhu and J. Zhu, *Small*, 2024, **20**, 2400615.

112 M. Velpandian, V. Dhongde, K. Singh, P. Gupta, D. Sarma, A. Mahata and S. Basu, *Chem. Eng. Res. Des.*, 2023, **198**, 1–13.

113 L. Lv, H. Tan, Y. Kong, B. Tang, Q. Ji, Y. Liu, C. Wang, Z. Zhuang, H. Wang, M. Ge, M. Fan, D. Wang and W. Yan, *Angew. Chem., Int. Ed.*, 2024, **63**, e202401943.

114 M. Yuan, J. Chen, Y. Bai, Z. Liu, J. Zhang, T. Zhao, Q. Shi, S. Li, X. Wang and G. Zhang, *Chem. Sci.*, 2021, **12**, 6048–6058.

115 Y. Wang, S. Xia, K. Chen, J. Zhang, C. Yu, J. Wu, P. Wang, W. Zhang and Y. Wu, *Angew. Chem., Int. Ed.*, 2025, **64**, e202503011.

116 Y. Yang, G. Wu, J. Jiang, W. Zhang, S. Liu, R. Yu, F. Liu, A. Du, L. Dai, X. Mao and Q. Qin, *Adv. Mater.*, 2024, **36**, 2409697.

117 Z. Feng, L. Zhang, Y. Guo, J. Guo, F. Li and F. Yu, *Angew. Chem., Int. Ed.*, 2025, **64**, e202500262.

118 Z.-S. Sun, X.-Y. Xiang, Q.-P. Zhao, Z. Tang, S.-Y. Jiang, T.-B. Lu, Z.-M. Zhang, B. Wang and H.-Q. Yin, *Chin. J. Catal.*, 2024, **65**, 153–162.

119 C. Zhao, Y. Jin, J. Yuan, Q. Hou, H. Li, X. Yan, H. Ou and G. Yang, *J. Am. Chem. Soc.*, 2025, **147**, 8871–8880.

120 Y. Zhao, Y. Ding, W. Li, C. Liu, Y. Li, Z. Zhao, Y. Shan, F. Li, L. Sun and F. Li, *Nat. Commun.*, 2023, **14**, 4491.

121 Y. Zhou, B. Yang, Z. Huang, G. Chen, J. Tang, M. Liu, X. Liu, R. Ma, Z. Mei and N. Zhang, *Appl. Catal., B*, 2024, **343**, 123577.

122 J. Ran, L. Wang, M. Si, X. Liang and D. Gao, *Small*, 2023, **19**, 2206367.

123 F. Raziq, K. Khan, S. Ali, S. Ali, H. Xu, I. Ali, A. Zada, P. Muhammad Ismail, A. Ali, H. Khan, X. Wu, Q. Kong, M. Zahoor, H. Xiao, X. Zu, S. Li and L. Qiao, *Chem. Eng. J.*, 2022, **446**, 137161.

124 F. Li, W. Zhang, P. Zhang, C. Li, D. Fang, F. Shen and K. Li, *Sci. Adv.*, 2025, **357**, 129997.

125 J. Zhang, Y. Ye, B. Wei, F. Hu, L. Sui, H. Xiao, L. Gui, J. Sun, B. He and L. Zhao, *Appl. Catal., B*, 2023, **330**, 122661.

126 S. She, J. Yu, W. Tang, Y. Zhu, Y. Chen, J. Sunarso, W. Zhou and Z. Shao, *ACS Appl. Mater. Interfaces*, 2018, **10**, 11715–11721.

127 X. Sun, Y. Yuan, S. Liu, H. Zhao, S. Yao, Y. Sun, M. Zhang, Y. Liu and Z. Lin, *Adv. Funct. Mater.*, 2025, **35**, 2416705.

128 W. Zhang, F. Li, W. Zhang, Y. Wang, S. Liu, X. Mo and K. Li, *Sci. Adv.*, 2023, **317**, 123775.

129 Y. Li, Y. Zhang, L. Shi, X. Liu, Z. Zhang, M. Xie, Y. Dong, H. Jiang, Y. Zhu and J. Zhu, *Small*, 2024, **20**, 2402823.

130 G. Dong, G. Wang, J. Cheng, M. Li, Z. Liang, D. Geng and W. Tang, *Appl. Catal., B*, 2024, **342**, 123444.

131 S. She, Y. Zhu, X. Wu, Z. Hu, A. Shelke, W. Pong, Y. Chen, Y. Song, M. Liang, C. Chen, H. Wang, W. Zhou and Z. Shao, *Adv. Funct. Mater.*, 2022, **32**, 2111091.

132 Y. Liu, C. Ye, S. Zhao, Y. Wu, C. Liu, J. Huang, L. Xue, J. Sun, W. Zhang, X. Wang, P. Xiong and J. Zhu, *Nano Energy*, 2022, **99**, 107344.

133 X. Wei, C. Chen, X. Fu and S. Wang, *Adv. Energy Mater.*, 2024, **14**, 2303027.

134 K. Zhu, F. Shi, X. Zhu and W. Yang, *Nano Energy*, 2020, **73**, 104761.

135 X. Wei, X. Wen, Y. Liu, C. Chen, C. Xie, D. Wang, M. Qiu, N. He, P. Zhou, W. Chen, J. Cheng, H. Lin, J. Jia, X. Fu and S. Wang, *J. Am. Chem. Soc.*, 2022, **144**, 11530–11535.

136 B. Mishra, S. Biswal, M. Ussama, M. Ali Haider and B. Tripathi, *Appl. Catal., B*, 2024, **342**, 123395.

137 D. Chen, C. Chen, Z. M. Baiyee, Z. Shao and F. Ciucci, *Chem. Rev.*, 2015, **115**, 9869–9921.

138 K. Chu, J. Qin, H. Zhu, M. De Ras, C. Wang, L. Xiong, L. Zhang, N. Zhang, J. Martens, J. Hofkens, F. Lai and T. Liu, *Sci. China Mater.*, 2022, **65**, 2711–2720.

139 L. Yang, Z. Lin, C. Yu, M. Liao, Y. Liu, S. Lv, G. Wang, X. Peng, G. He and H. Cheng, *J. Mater. Sci. Technol.*, 2026, **245**, 164–174.

140 X. Li, X. Wang, Y. Wang, J. Shao, Y. Wu, S. Jana, H. Liu, Y. Peng, Z. Wu, Z. Li, Y. Cong, Y. Zhang, G. Li and L. Li, *Angew. Chem., Int. Ed.*, 2025, **64**, e202424347.

141 J. Zhu, Y. Wang, A. Zhi, Z. Chen, L. Shi, Z. Zhang, Y. Zhang, Y. Zhu, X. Qiu, X. Tian, X. Bai, Y. Zhang and Y. Zhu, *Angew. Chem., Int. Ed.*, 2022, **61**, e202111670.

142 K. Wang, X. Guo, C. Han, L. Liu, Z. Wang, L. Thomsen, P. Chen, Z. Shao, X. Wang, F. Xie, G. Liu, L. Wang and S. Liu, *ACS Nano*, 2025, **19**, 3818–3829.

143 Y. Zhang, S. Zhang, N. Hu, Y. Liu, J. Ma, P. Han, Z. Hu, X. Wang and G. Cui, *Chem. Soc. Rev.*, 2024, **53**, 3302–3326.

144 P. Liang, D. Meng, Y. Liang, Z. Wang, C. Zhang, S. Wang and Z. Zhang, *Chem. Eng. J.*, 2021, **409**, 128196.

145 X. Kuai, G. Yang, Y. Chen, H. Sun, J. Dai, Y. Song, R. Ran, W. Wang, W. Zhou and Z. Shao, *Adv. Energy Mater.*, 2019, **9**, 1902384.

146 M. Krishnamachari, S. Lenus, K. Pradeeswari, R. Arun pandian, M. Kumar, J. Chang, S. p. Muthu, R. Perumalsamy, Z. Dai and P. Vijayakumar, *ACS Appl. Nano Mater.*, 2023, **6**, 16106–16139.

147 Y. Zhang, F. Gao, D. Wang, Z. Li, X. Wang, C. Wang, K. Zhang and Y. Du, *Coord. Chem. Rev.*, 2023, **475**, 214916.

148 X. Luo, X. Tan, P. Ji, L. Chen, J. Yu and S. Mu, *EnergyChem*, 2023, **5**, 100091.

149 M. Xu, S. Dong, H. Guo, Z. Tao, Y. Jeon, Z. Zhang, Z. Chen, H. Su, Z. Liu, Y. Lin, J. Irvine, T. Li and D. Chen, *Appl. Catal., B*, 2025, **375**, 125433.

150 X. Chen, G. Ren, Y. Wang, Z. Li, Z. Zhang and X. Meng, *Appl. Catal., B*, 2024, **355**, 124173.

151 Q. Tang, Q. Hao, Q. Zhu, J. Wu, K. Huang, K. Liu and J. Lu, *Adv. Energy Mater.*, 2025, **15**, 2403778.

152 U. Kim, S. Lee, D. Koo, Y. Choi, H. Kim, E. Son, J. M. Baik, Y. Han and H. Park, *ACS Energy Lett.*, 2023, **8**, 1575–1583.

153 D. Liu, P. Zhou, H. Bai, H. Ai, X. Du, M. Chen, D. Liu, W. Ip, K. H. Lo, C. Kwok, S. Chen, S. Wang, G. Xing, X. Wang and H. Pan, *Small*, 2021, **17**, 2101605.

154 S. Qu, H. Huang, J. Wang, P. Cui, Y. Li, M. Wang, L. Li, F. Yang, C. Sun, Q. Zhang, P. Zhu, Y. Wang and M. Li, *Angew. Chem., Int. Ed.*, 2025, **64**, e202415949.